
HOW DIFFUSION PRIOR LANDSCAPES SHAPE THE POSTERIOR IN BLIND DECONVOLUTION

A PREPRINT

 **Minh-Hai Nguyen***
 IRIT
 Toulouse University
 France
 minh-hai.nguyen@irit.fr

Edouard Pauwels
 Toulouse School of Economics
 Université Toulouse Capitole and IUF
 France
 edouard2.pauwels@ut-capitole.fr

Pierre Weiss
 IRIT
 Toulouse University, CNRS
 France
 pierre.armand.weiss@gmail.com

ABSTRACT

The Maximum A Posteriori (MAP) estimation is a widely used framework in blind deconvolution to recover sharp images from blurred observations. The estimated image and blur filter are defined as the maximizer of the posterior distribution. However, when paired with sparsity-promoting image priors, MAP estimation has been shown to favors blurry solutions, limiting its effectiveness. In this paper, we revisit this result using diffusion-based priors, a class of models that capture realistic image distributions. Through an empirical examination of the prior's likelihood landscape, we uncover two key properties: first, blurry images tend to have higher likelihoods; second, the landscape contains numerous local minimizers that correspond to natural images. Building on these insights, we provide a theoretical analysis of the blind deblurring posterior. This reveals that the MAP estimator tends to produce sharp filters (close to the Dirac delta function) and blurry solutions. However local minimizers of the posterior, which can be obtained with gradient descent, correspond to realistic, natural images, effectively solving the blind deconvolution problem. Our findings suggest that overcoming MAP's limitations requires good local initialization to local minima in the posterior landscape. We validate our analysis with numerical experiments, demonstrating the practical implications of our insights for designing improved priors and optimization techniques.

Keywords diffusion models, blind deconvolution, maximum a posteriori, learned prior landscape

1 Introduction

Blind image deconvolution consists in recovering a sharp image \bar{x} and a degradation kernel \bar{h} , from a blurry observation y given by

$$y = \bar{h} \star \bar{x} + b \tag{1}$$

where \star denotes convolution operator and b is some noise. This problem is fundamental in areas such as biomedical imaging, astronomy, and computer vision. The blur can result from various physical mechanisms including diffraction, turbulence, defocus and motion blur. In all cases, these effects can significantly degrade image quality and hinder interpretability.

Taking a Bayesian viewpoint, we assume that \bar{x} and \bar{h} are realizations of two *independent* random vectors x and h with prior distributions p_x and p_h . Using the Bayes's formula, the posterior distribution of the image and kernel given the

* <https://mh-nguyen712.github.io/>

observation y can be written as:

$$p(x, h|y) = \frac{p(y|x, h)p_x(x)p_h(h)}{p(y)}. \quad (2)$$

Under the assumption that the noise $b \sim \mathcal{N}(0, \sigma_y^2 \text{Id})$ is white and Gaussian, the likelihood has the explicit form $p(y|x, h) \sim \mathcal{N}(y|h \star x, \sigma_y^2 \text{Id})$. Therefore, the negative-log-posterior can be written as:

$$-\log p(x, h|y) \propto \frac{\|h \star x - y\|_2^2}{2\sigma_y^2} - \log p_x(x) - \log p_h(h). \quad (3)$$

Arguably the most popular estimator in the literature is the Maximum A Posteriori (MAP), which seeks to maximize the posterior $p(x, h|y)$, or equivalently minimize eq. (3) with respect to the image and kernel pair (x, h) .

Popular approaches for describing the kernel prior p_h include a direct modeling in the pixel domain with non-negativity and normalization constraints (simplex) [Chan and Wong, 1998, Pan et al., 2014], more specific parametric models such as linear motion and out-of-focus blurs [Oliveira et al., 2013] or richer diffraction-limited families [Shajkofci and Liebling, 2020, Debarnot and Weiss, 2024].

The choice of an image potential p_x is crucial, with past approaches often promoting sparsity in the spatial [Pan et al., 2016, Ge et al., 2011, Pan et al., 2014], wavelet [Jalobeanu et al., 2002, Pustelnik et al., 2016], or gradient domains [Pan et al., 2014, Chan and Wong, 1998, Anger et al., 2019]. However, these handcrafted priors were found [Levin et al., 2009, Rameshan et al., 2012, Perrone and Favaro, 2014, Benichoux et al., 2013] to suffer from serious flaws, with the global minimizer of the negative log-posterior often corresponding to the “no-blur” solution. That is a Dirac kernel and blurry image. Other contributions have argued that the true image and kernel can sometimes be found at a local minimizer of (3), rehabilitating the idea that local minimizers of the posterior (3) could be useful for blind deblurring [Benichoux et al., 2013, Rameshan et al., 2012]. Numerical methods have also been proposed in these works to find a local minimizer instead of the no-blur solution, by using a well-designed initialization strategy.

Recent advances in generative modeling [Rombach et al., 2022, Ramesh et al., 2021, Karras et al., 2019], particularly in variational auto-encoders [Kingma and Welling, 2014], normalizing flows [Rezende and Mohamed, 2015], and diffusion models [Song et al., 2020], have demonstrated unprecedented capability in capturing the complexity of natural images through learned priors. This progress naturally raises the question: *Can diffusion priors rehabilitate the MAP approach for blind deblurring?*

Contributions This paper addresses the above question through rigorous theoretical analysis and comprehensive empirical validation. To summarize, our contributions are as follows:

1. We study the landscape of diffusion priors and reveal two key insights about state-of-the-art learned diffusion priors: first, they consistently assign higher likelihood to blurry images than to sharp ones, and second, natural images reside in deep “valleys” of the potential landscape—a property aligned with the well-established observation that images lie on low-dimensional manifolds.
2. Based on these findings, we show that even with state-of-the-art diffusion priors, the MAP estimator still promotes the no-blur solution, suggesting a fundamental limitation of the approach.
3. However, under proper convolution filter parameterization, we show that local minima of the prior are stable local minima of the posterior. Based on empirical observation, we also propose an initialization strategy to prevent the convergence to the no-blur solution.
4. We validate these theoretical findings and the proposed initialization strategy through extensive numerical experiments, demonstrating their practical significance for blind deblurring applications. The code to reproduce the numerical experiments is available at https://github.com/mh-nguyen712/blind_deblur_diffusion.

The paper is organized as follows. In section 2, we present the background on diffusion priors and conduct a preliminary experimental exploration of their landscape. In section 3, we provide a theoretical analysis of the MAP estimator and local minima of the posterior. In section 4, we validate our theoretical findings through numerical experiments. Based on these analyses, we propose in section 5 an initialization strategy to avoid the no-blur solution with numerical results in various use cases, the conclusions are drawn in section 6.

2 Diffusion prior landscapes

In this section, we describe diffusion priors and conduct a preliminary experimental exploration of their landscape. We begin with a brief overview of diffusion models and outline how to use them to evaluate a prior likelihood. We

then reveal two key properties of learned diffusion potentials – $\log p_{\mathbf{x}}$: first, natural images lie on low dimensional structures of the learned potential, which is consistent with previous observations [Pope et al.]; second, they tend to assign higher likelihoods to blurry images over sharper ones.

2.1 Diffusion based potentials

Diffusion models Diffusion models are powerful generative models and based on the following stochastic differential equation (SDE) on \mathbb{R}^d [Song et al., 2020]:

$$d\mathbf{x}_t = f(\mathbf{x}_t, t) dt + g(t) d\mathbf{w}_t, \quad (4)$$

where \mathbf{w}_t is the standard Brownian process, $f: \mathbb{R}^d \times \mathbb{R} \rightarrow \mathbb{R}^d$ denotes a drift term and $g: \mathbb{R} \rightarrow \mathbb{R}$ denotes a diffusion coefficient. The choice of f and g define the diffusion process, with various qualitative properties [Song et al., 2020, Karras et al., 2022]. In this model, \mathbf{x}_0 follows the clean image distribution $p_{\mathbf{x}}$. For long time horizon T and under technical conditions, the solution of the SDE \mathbf{x}_T approximately follows a normal distribution with no information left on $p_{\mathbf{x}}$, whose parameters depend on f and g . This process can be reversed [Anderson, 1982] using the following SDE running backward in time, which serves as a generative process:

$$d\mathbf{x}_t = [f(\mathbf{x}_t, t) - g(t)^2 \nabla \log p_t(\mathbf{x}_t)] dt + g(t) d\mathbf{w}_t. \quad (5)$$

Here p_t denotes the density at time t and the solutions to this reversed-time SDE are distributed according to $p_{\mathbf{x}}$ at time $t = 0$. To generate new samples, we start from $\mathbf{x}_T \sim \mathcal{N}(0, \text{Id})$ and solve the backward SDE eq. (5) for $t \in [T, 0]$ by a discretization scheme, e.g., Euler-Maruyama. Training a diffusion model amounts to estimating the Stein’s score function of each marginal distribution, $\nabla \log p_t$, by score matching [Vincent, 2011]. The score $\nabla \log p_t$ is typically parameterized by a time-dependent neural network $s_{\theta}(\cdot, t)$.

In what follows, we let $q_t \stackrel{\text{def}}{=} -\log p_t$ denote the potential (negative-log-prior) term. We evaluate potentials with a small value of time $t_{\epsilon} = 10^{-3}$, to obtain an approximation of $-\log p_0 = -\log p_{\mathbf{x}}$. This is needed for numerical stability [Song et al., 2020]. In what follows, we simply write q to denote $-\log p_{t_{\epsilon}}$, and we subsequently use $\nabla q(\cdot)$ to describe the action of the neural network $-s_{\theta}(\cdot, t_{\epsilon})$. This quantity is proportional to a difference between a noisy image and its denoised version via Tweedie’s formula [Vincent, 2011].

Likelihood computation There exists a *deterministic process* with trajectories sharing the same marginal distribution as the SDE in (4). It can be obtained by the Fokker-Plank equation and it is defined by the following ordinary differential equation (ODE) [Song et al., 2020, Karras et al., 2022]:

$$d\mathbf{x}_t = v(\mathbf{x}_t, t) dt, \quad \text{where } v(\mathbf{x}_t, t) \stackrel{\text{def}}{=} f(\mathbf{x}_t, t) + \frac{1}{2} g(t)^2 \nabla q_t(\mathbf{x}_t). \quad (6)$$

If $\mathbf{x}_0 \sim p_{\mathbf{x}}$, then the trajectory \mathbf{x}_t satisfies $\mathbf{x}_t \sim p_t(\mathbf{x}_t)$ for all $t \in [0, T]$. We can compute the potential of an image x_0 with the instantaneous change of variables formula [Chen et al., 2018]:

$$-\log p_{\mathbf{x}}(x_0) = -\log p_T(x_T) - \int_0^T \nabla \cdot v(x_t, t) dt, \quad (7)$$

where x_t is the trajectory of the ODE in eq. (6). The divergence term $\nabla \cdot v(x_t, t)$ can be approximated by the Skilling-Hutchinson trace estimator [Skilling, 1989]:

$$\nabla \cdot v(x_t, t) = \mathbb{E}_{\mathbf{u}} [\mathbf{u}^T J_v(x_t, t) \mathbf{u}],$$

where J_v is the Jacobian of $v(\cdot, t)$, and \mathbf{u} is a random variable with zero mean and identity covariance. In our implementation, we use a Rademacher random variable. The vector-Jacobian product $\mathbf{u}^T J_v(x_t, t)$ is computed using reverse-mode automatic differentiation with roughly the same cost as evaluating $v(x_t, t)$. The Skilling-Hutchinson trace estimator is unbiased so by averaging multiple runs, we can approximate the divergence. The integral can be evaluated using numerical ODE solver. Finally, at time T , the random variable \mathbf{x}_T follows a Gaussian distribution with zero mean and standard deviation $\sigma(T)$ (depending on the model and on the dataset), which allows us to compute the term $\log p_T(x_T)$ in eq. (7).

In all of our experiments, we use the Runge-Kutta 45 numerical scheme, provided by `scipy.integrate.solve_ivp` with tolerance value `atol=1e-5` and `rtol=1e-5`. We use a similar implementation to [Song et al., 2020], but we compute the exact value of the potential instead of the bit-ber-dim value in the original implementation. This process is numerically intensive, as it requires hundreds of evaluations of the neural network ∇q_t .

Datasets, pretrained models and implementation details We use a model² trained on the 256×256 FFHQ dataset from Song *et al.* [Song et al., 2020] and three models³ trained on the ImageNet, FFHQ and AFHQ datasets at a 64×64

²Pre-trained model: https://github.com/yang-song/score_sde_pytorch

³Pre-trained model: <https://github.com/NVlabs/edm>

resolution from the widely used EDM framework by Karras *et al.* [Karras et al., 2022]. The latter are more recent and produce higher quality images. For brevity, we refer to these models throughout the paper as FFHQ-256, ImageNet-64, FFHQ-64, and AFHQ-64 respectively. ImageNet-64 is a class-conditional model, throughout the paper, we use the first 10 classes of the ImageNet dataset. We summarize the pre-trained models used in this paper in table 1.

Table 1: Pre-trained diffusion models used in our study. The computation time was evaluated using a single NVIDIA V100 SMX2-16GB GPU and with 10 CPU cores from an Intel Cascade Lake 6248 processor.

Pre-trained model	FFHQ-256 [Song et al., 2020]	ImageNet-64 [Karras et al., 2022]	FFHQ-64 [Karras et al., 2022]	AFHQ-64 [Karras et al., 2022]
Train dataset	FFHQ	ImageNet	FFHQ	AFHQ
SDE/ODE formulation	VE SDE	EDM	EDM	EDM
Resolution	$256 \times 256 \times 3$	$64 \times 64 \times 3$	$64 \times 64 \times 3$	$64 \times 64 \times 3$
Num. parameters (million)	66	296	63	63
Model eval. (sec./image)	0.036	0.014	0.006	0.006
Potential eval. (sec./image)	8.461	10.26	5.05	5.05

2.2 Manifold hypothesis

It is now rather well established that natural images live on low-dimensional structures [Pope et al.]. In this part, we explore whether diffusion based priors capture this property and provide some additional insights on the potential’s landscape.

Gradient descent for computing critical points of the potential We first perform a gradient descent on the potential using the ∇q (provided by pre-trained score model). We start either from natural images x_i belonging to the dataset used to train the diffusion model, from images from other unrelated dataset, or from pure white Gaussian noise. The descent trajectories starting from x_i end at near critical points \bar{x}_i that satisfy $\nabla q(\bar{x}_i) \approx 0$. Generically, critical points obtained by gradient descents are second-order critical points [Lee et al., 2016a], that is, points where the gradient vanishes and the Hessian matrix is positive semi-definite. They are computed by performing 10k descent steps on 64×64 resolution models and 5k descent steps on FFHQ-256, with a fixed step-size of 0.02. In fig. 1, we illustrate that the critical points \bar{x}_i can be seen as denoised versions of the initial points x_i . We track the value of the potential $q(\cdot)$ along the iterations to verify that it does not vary at the end of the optimization process in fig. 2.



Figure 1: Critical points obtained by a gradient descent starting from real images in FFHQ-256 using the FFHQ-256 potential. The critical points behave as denoised versions of the initial image. The potential $q = -\log p_x$ displayed on the top of each image is about twice lower for critical points.

Prior’s landscape around critical points In fig. 3, we show the box-plots of relative distance between x_i and \bar{x}_i and the variation of the potential associated to those points. The relative distance $\frac{\|x - \bar{x}\|}{\|\bar{x}\|}$ varies by less than 5% in average both when starting with noise and natural images. This suggests that a wide variety of images, whether natural or artificial, tend to be situated near critical points in the prior’s landscape. The situation for the potential is different: the noise has a much higher potential than natural images, meaning that diffusion priors can clearly distinguish them. Also, the difference of potential $q(x) - q(\bar{x})$ between the initialization and the found critical point is much higher for natural images than for the noisy image. This suggests that the prior landscape curvature is high around natural images.

In fact, let $d = \frac{x - \bar{x}}{\|x - \bar{x}\|}$ denote the direction linking x to \bar{x} and let $q^d(s) \stackrel{\text{def}}{=} q(\bar{x} + s \cdot d)$ denote the 1D profile of the potential along the direction d . The local curvature of the prior at \bar{x} in the direction d can be defined as:

$$(q^d)''(s) = \langle \nabla^2 q(\bar{x})d, d \rangle.$$

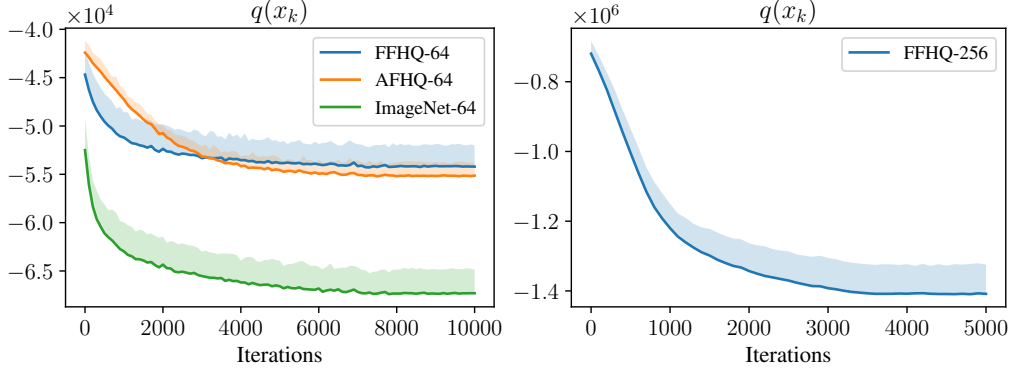


Figure 2: Illustration of the convergence of a gradient descent on the potential q using different models. The potential stabilizes after a few thousands iterations.

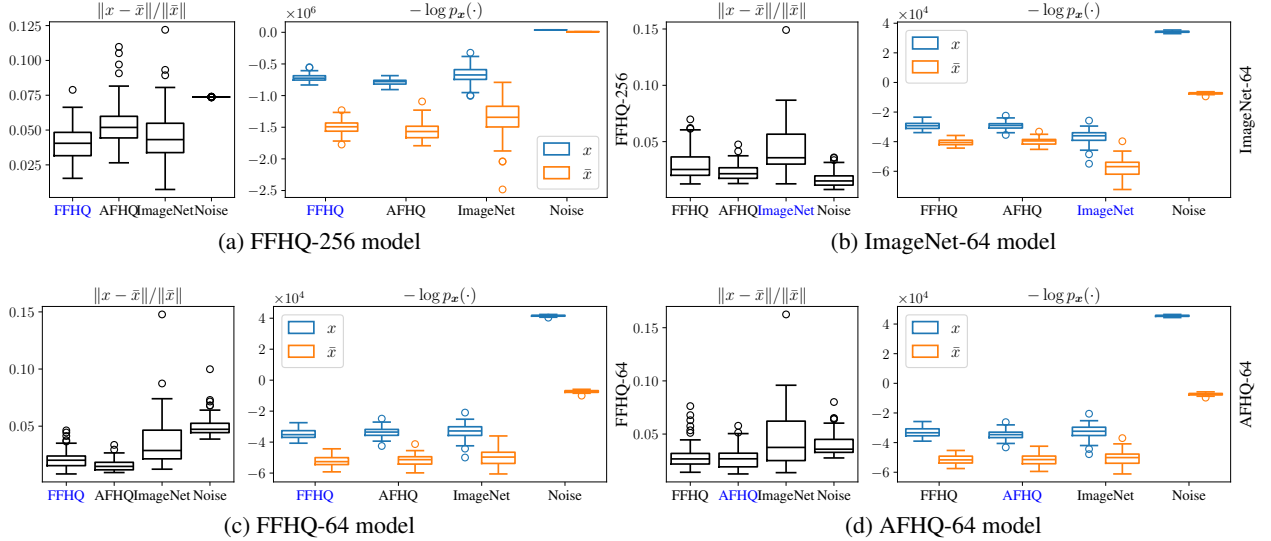


Figure 3: Distance and difference of potential between natural images and the corresponding critical points. The dataset used to train the model is highlighted in blue. Observe that the relative distance between the critical points and the initial images is less than 10% even when starting from pure noise. Yet, the potential is much lower.

Indeed, the facts that $\nabla q(\bar{x}) = 0$ and $q(x) \gg q(\bar{x})$ with x close to \bar{x} implies that there is a large curvature in the direction $\bar{x} - x$ as otherwise, $q(x)$ would be close to $q(\bar{x})$. This is fully consistent with the concept of a (local) image manifold: the potential blows up in directions that do not preserve an image-like structure such as noise, but does not vary too much along the image manifold.

Spectra of the Hessian of the potential To further validate this intuition, we can compute the whole spectrum of the Hessian matrix $\nabla^2 q$ at some critical points \bar{x}_i . The intrinsic dimension of the local image manifold – corresponds to the number of “small” eigenvalues.

Suppose that $q : \mathbb{R}^d \rightarrow \mathbb{R}$ is a \mathcal{C}^2 function, then $\nabla q : \mathbb{R}^d \rightarrow \mathbb{R}^d$ is a \mathcal{C}^1 function. For any $\bar{x} \in \mathbb{R}^d$, we have:

$$\nabla^2 q(\bar{x}) = \begin{pmatrix} \nabla^2 q(\bar{x}) \cdot e_1 \\ \vdots \\ \nabla^2 q(\bar{x}) \cdot e_d \end{pmatrix} \in \mathbb{R}^{d \times d},$$

where (e_1, \dots, e_d) is the canonical basis of \mathbb{R}^d . Since the gradient $\nabla q(\bar{x})$ is parameterized by a neural network, its evaluation corresponds to a single forward pass. Computing the product $\nabla^2 q(\bar{x}) \cdot e_k$ corresponds to performing the Jacobian-vector product on the neural network ∇q . This can be done seamlessly using two consecutive backward derivative computation as implemented in the Pytorch library [Paszke et al., 2019], in the function `torch.autograd.functional.jvp`.

We build the full Hessian matrix $\nabla^2 q(\bar{x})$ by iteratively performing the Jacobian-vector product for all directions, which results in a dense matrix of size $d \times d$. For models at a 64×64 resolution, we have $d = 3 \cdot 64 \cdot 64 = 12288$. We then compute its singular values by `torch.linalg.svdvals`, in double precision floating-point format.

This is a heavy computational procedure, since the score ∇q needs to be differentiated along all directions: the number of calls to compute the Hessian-vector product by the automatic differentiation equals the number of pixels in the image. Hence, we limited our analysis to small $64 \times 64 \times 3$ images and the spectra are shown in fig. 4. Only a small portion of the eigenvalues are low, which is consistent with the concept of a low dimensional structure encompassing natural images. This experiment confirms the findings in [Pope et al.] about the intrinsic dimension of images, with a different computational approach. After finishing this manuscript, J. Pidstrigach [Pidstrigach, 2022] indicated us that the authors in [Stanczuk et al., 2024] proposed an approach with a similar flavor.

Overall, the experiments in this paragraph suggest the following phenomenon: the potential q is erratic, with critical points near every point in space. It possesses a deep and low-dimensional valley, which can be thought of as a manifold of natural images.

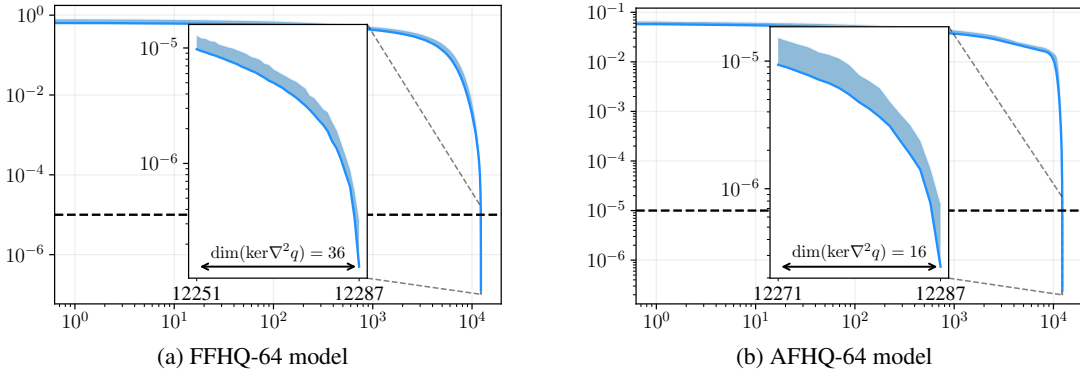


Figure 4: Spectra of the Hessian of the potential $\nabla^2 q(\bar{x}_i)$ for 20 different critical points \bar{x}_i . By thresholding all values below 10^{-5} , the local image manifold dimension is estimated at 36 for FFHQ-64 and 16 for AFHQ-64.

2.3 Blurry images are more likely

A key property that explains the failure of the MAP estimate when used with sparsity-based priors is that blurry images are more likely than sharper ones. This phenomenon can be proven for TV-based and sparsity-based priors using Hölder type inequalities [Levin et al., 2009, Perrone and Favaro, 2014, Benichoux et al., 2013]. In this section, we aim to investigate whether this property holds for diffusion model priors as well.

Measuring the potential of blurry images We consider a collection of sharp images and convolve them with four different types of blurs: Gaussian, motion, Airy disk, and defocus, as illustrated in fig. 5. We let $\theta \mapsto h_\theta \in \mathbb{R}^N$ denote a parameterization of the blur kernel. We consider a 1D parameterization and the parameter θ roughly accounts for the kernel’s diameter in pixels and the spatial size of all kernels is 31×31 . Starting with an image x from the dataset, we measure the potential $q(h_\theta * x)$ for various values of θ (representing different levels of blur), as described in section 2.1. We discretize the parameter space $[0, \theta_{\max}]$ into an equally spaced grid of 11 points, where $\theta_{\max} = 5$ and $h_0 = \delta$ is the Dirac.

The results for 100 random images from the same training set, for various models are shown in fig. 7. We observe that the potential $q(h_\theta * x)$ decreases strictly with θ , indicating that blurry images are more likely. Qualitative results on a single image can be found in fig. 6. This observation demonstrates that shifting from handcrafted priors to more complex learned priors, does not affect the tendency to favor blurry images. This aligns with recent findings in [Karczewski et al., 2025], which show that cartoon-like structures or blurry images have higher likelihood, with a different approach for computing the likelihood.

A specificity of natural images To investigate further, we train a diffusion model similar as the one in [Song et al., 2020], but on the MNIST dataset with binary pixel values. The model used is a UNet2DModel from the Diffusers library⁴, configured for grayscale images at a 32×32 resolution, with `block_out_channels = [32, 64, 128,`

⁴<https://huggingface.co/docs/diffusers/en/api/models/unet2d>

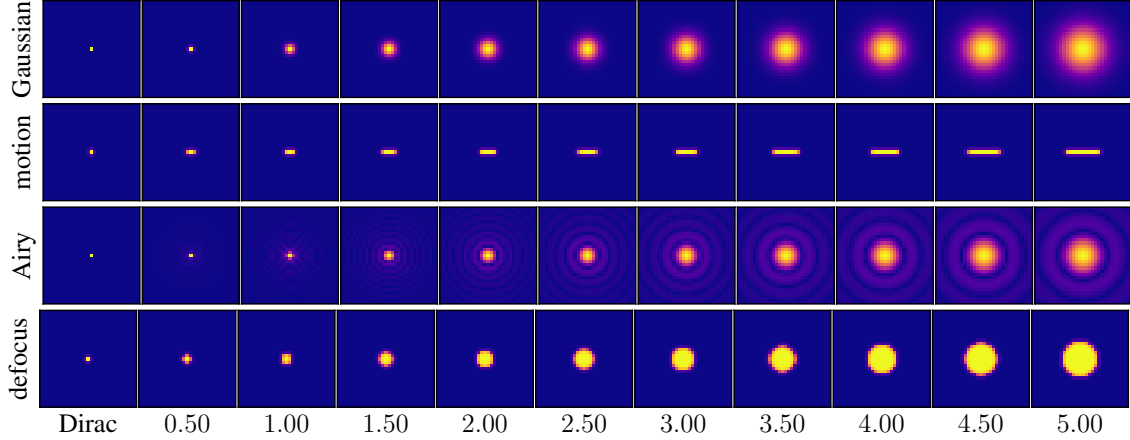


Figure 5: Different 1D blur families used in the forthcoming experiments. The parameter θ roughly accounts for the diameter of the PSF with $h_0 = \delta$ and the higher θ , the more blur.

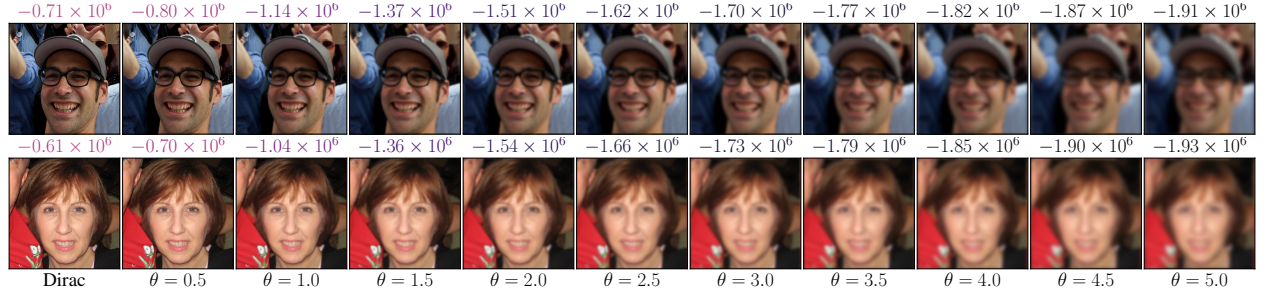


Figure 6: Variation of the potential q with Gaussian blur on the FFHQ-256 model. A smaller potential means a more likely image. Observe that the potential is decreasing strictly with the blur level θ .

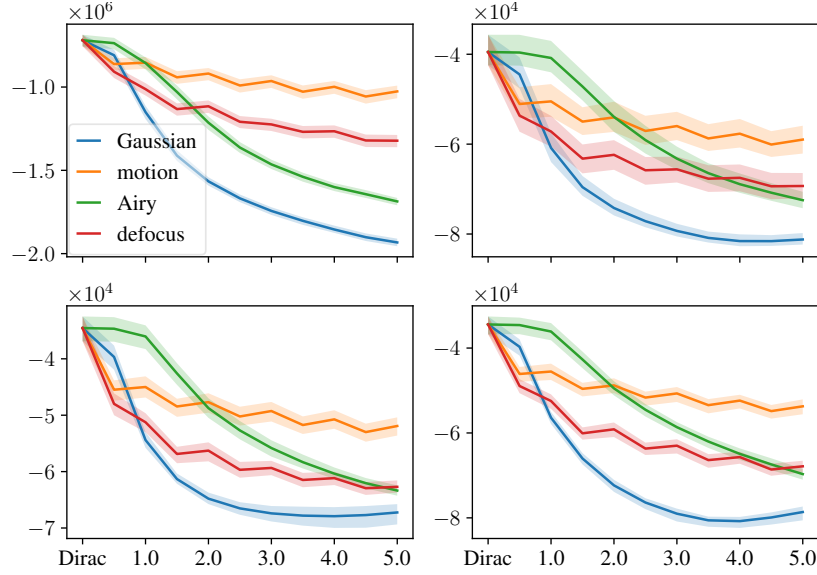


Figure 7: The evolution of the potential $q(h_\theta * x)$ on various models and 100 different images. From top-left to bottom-right: FFHQ-256, ImageNet-64, FFHQ-64 and AFHQ-64. The initial images are taken from the same training dataset as the pre-trained model. The potential is consistently decreasing with the blur level θ , meaning that blurry images are more likely.

256]. The model comprises 15.9 million parameters and was trained for 100 epochs (6 million images) using the VE-SDE formulation [Song et al., 2020]. We then repeat the above procedure, with the results shown in Fig. 8. In this

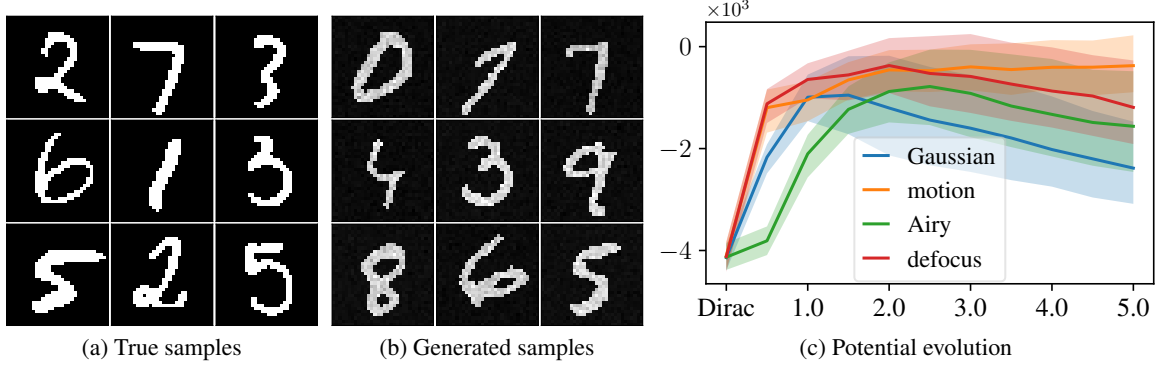


Figure 8: variation of the potential q with the blur level, for a model trained on a binarized MNIST dataset. The potential increases, suggesting that the property “more blurry=more likely” is a specificity of natural images and not a bias of the neural network architecture.

case, we observe that the potential tend to increase with the kernel size θ . This experiment suggests that the preference for blurry images is an inherent characteristic of models trained on natural images. In particular, it suggests that this tendency is not a consequence of the network architecture. One possible explanation for the fact that blurry images are more likely is that they predominantly consist of smooth regions separated by sharp boundaries, causing the smooth areas to be favored by the prior. Additionally, traditional computer vision databases contain photographs of objects with varying depths, with some regions suffering from defocus blur.

3 Theoretical analysis: posterior properties and recovery guarantees

In this section, we suppose that the parameterization of the family of blur kernels $\theta \in \mathbb{R}^P \mapsto h_\theta \in \mathbb{R}^N$ is twice continuously differentiable. We let $H_\theta : x \mapsto h_\theta \star x$ denote the corresponding convolution operator and suppose that θ is uniformly distributed in a compact set $\Theta \subset \mathbb{R}^P$. By doing so, we implicitly define a probability distribution on the convolution kernels. The mapping h_θ can be thought of as a transport map from a uniform distribution to a distribution of convolution kernels. The negative log-posterior eq. (3) simplifies to:

$$\ell_y(x, \theta) \stackrel{\text{def}}{=} \frac{1}{2} \|H_\theta x - y\|^2 + \sigma_y^2 q(x). \quad (8)$$

3.1 MAP solutions are blurry

Levin *et al.* [Levin et al., 2009] have shown that the set of global minimizers of eq. (8) with a total variation prior, contains the Dirac kernel and the MAP denoised image. However, their arguments relied on a basic scaling approach that does not hold when the kernel belongs to a constrained family. The arguments were later refined in [Perrone and Favaro, 2014] with a simplex constraint. In theorem 1, we propose a simple sufficient condition under which the same conclusion holds for arbitrary potentials, beyond handcrafted priors.

Theorem 1. *Let $\mathcal{H} = \{h_\theta, \theta \in \mathbb{R}^P\}$ denote the set of blur kernels. If the Dirac delta function $\delta \in \mathcal{H}$ and for any image x and kernel $h \in \mathcal{H}$,*

$$q(h \star x) \leq q(x), \quad (9)$$

then the set of global minimizers of eq. (8), if non-empty, contains the Dirac kernel and the MAP denoised image (see appendix A.1).

Though the proof (see appendix A.1) is relatively direct, identifying condition eq. (9) as the key mechanism for MAP failure is not obvious a priori. This result uncovers a fundamental mechanism behind MAP blind deblurring failures. Our numerical investigations in section 2.3 empirically validate this sufficient condition for diffusion-based potentials and natural images.

In section 4, we examine the 1D profile of the posterior, which shows that the global minimizer of the posterior coincides with the no-blur solution, as predicted by theorem 1. Therefore, our result provides a simple explanation (blurry images

are favored by the prior) to the empirical observation that blind deblurring with the MAP estimator results in the no-blur solution.

Remark 2. While the decay assumption eq. (9) seems valid for natural images x and kernels h_θ in the family \mathcal{H} , it appears to not be true for all possible images. In particular, if the potential q admits strict local minimizers \bar{x}_i and if h_θ is close to the Dirac mass, then $\|H_\theta \bar{x}_i - \bar{x}_i\|$ is small and $q(\bar{x}_i) < q(H_\theta \bar{x}_i)$. In the next section, we will show that the set of local minimizers of the potential indeed play a critical role for posterior maximization.

3.2 Local minimizers of the posterior

Stable recovery is one of the most important questions in blind inverse problems. Previous contributions [Ahmed et al., 2013, Lee et al., 2016b, Kech and Krahmer, 2017] provided sharp and elegant results. However, these cannot be applied to modern image priors as they require convex or sparse priors, random subspace constraints on the operator, *etc.* In this section, we establish general conditions on the prior and the operator that ensure the existence of a local minimizer of the posterior near the true image-kernel pair at low noise levels.

3.2.1 Main theoretical result

The main result of this section says roughly that, for blind deconvolution, second-order critical points of the prior are stable local minima of the posterior, under proper parameterization of the convolution kernel. Let us start with the main definition.

Definition 3 (Second-order critical points). An image \bar{x} is called a second-order critical point of the potential q if:

$$\nabla q(\bar{x}) = 0 \quad \text{and} \quad \nabla^2 q(\bar{x}) \succeq 0.$$

We first state the recovery result for second-order critical points in noiseless regime ($\sigma_y = 0$) in theorem 4 and then extend the result to the noisy case ($\sigma_y > 0$) in theorem 5. The proofs are postponed to appendix A.2.

Theorem 4 (Noiseless recovery). *Let $\bar{x} \in \mathbb{R}^N$ be a second-order critical point of q , $\bar{y} \in \mathbb{R}^N$ and $\bar{\theta} \in \mathbb{R}^P$ such that $h_{\bar{\theta}} \star \bar{x} = \bar{y}$. For all $\theta \in \mathbb{R}^P$, we let $J(\theta) = \frac{\partial}{\partial \theta}(h_\theta \star \bar{x}) \in \mathbb{R}^{N \times P}$ denote the Jacobian matrix. Under the following assumptions:*

$$\ker \nabla^2 q(\bar{x}) \cap \ker H_{\bar{\theta}} = \{0\}, \quad (10)$$

$$\ker J(\bar{\theta}) = \{0\}, \quad (11)$$

$$(h_{\bar{\theta}} \star \ker \nabla^2 q(\bar{x})) \cap \text{Im } J(\bar{\theta}) = \{0\}. \quad (12)$$

the couple $(\bar{x}, \bar{\theta})$ is a strict local minimizer of the noiseless cost function $\ell_{\bar{y}}$ with $\nabla^2 \ell_{\bar{y}}(\bar{x}, \bar{\theta})$ positive-definite.

Corollary 5 (Stable recovery). *Under the hypotheses of theorem 4, for any $\sigma_y > 0$, there exists $r, \epsilon > 0$ such that for any noise b with $\|b\| \leq \epsilon$, there is a unique minimizer (x_b^*, θ_b^*) of $\ell_{\bar{y}+b}$ in the ball of radius r around $(\bar{x}, \bar{\theta})$ with*

$$\|x_b^* - \bar{x}\| = \mathcal{O}(\|b\|) \quad \text{and} \quad \|\theta_b^* - \bar{\theta}\| = \mathcal{O}(\|b\|).$$

3.2.2 Significance of theorem 4 and theorem 5

General recovery guarantee theorem 4 and theorem 5 precisely characterize images that can be recovered: second-order critical points of the prior, such as local minima. This can be understood as a kind of compressed sensing type results [Ahmed et al., 2013, Lee et al., 2016b, Kech and Krahmer, 2017] that accommodates arbitrary priors and focuses on local (not global) minimizers. Recovery guarantees with generic learned priors remain largely unexplored, and our analysis significantly extends results such as [Bora et al., 2017], which are limited to points within a generator's range. Note that the width of the basin of attraction is crucial; we empirically analyze it in the coming sections.

Practical impact Theorem 4 provides a positive result: it ensures that properly initialized gradient descents can converge to the desired solution in blind deconvolution. However, this claim must be tempered by the fact that the true MAP solution — corresponding to the global minimizer of the posterior — which could be the degenerate no-blur solution, as established in theorem 1 and empirically observed in section 4.

For a given \bar{y} , theorem 4 also characterizes a class of image-kernel pairs that act as posterior local minima, making them potential MAP candidates recoverable by gradient-based methods. Importantly, multiple such pairs may exist for the same \bar{y} , including the correct solution as well as the no-blur solution from theorem 1.

This analysis highlights a critical limitation: even with modern learned priors, global MAP solutions can remain suboptimal. Furthermore, while favorable local minima do exist, they may be challenging to reach or distinguish from undesirable solutions.

This insight is valuable for MAP-based blind deblurring methods. Beyond the characterization of posterior local minima, our theory helps explain why vanilla MAP estimation is almost always combined with additional heuristics to avoid the failure of global MAP optimization. Indeed, state-of-the-art blind deblurring algorithms using diffusion priors rely on such modifications: [Chung et al., 2023] adds an ℓ_0/ℓ_1 regularization, [Chihaoui et al., 2024] introduces a norm constraint on latent variables, and [Li et al., 2024, Sanghvi et al., 2025, Laroche et al., 2024] optimize a marginalized (over x) posterior $p(h|y)$ rather than the joint posterior.

Our findings suggest the possibility of developing a general theory to support these empirical strategies. They also motivate a simple initialization procedure, which we introduce in the next section.

3.2.3 Interpretation of the conditions

The conditions in theorem 4 require careful interpretation. To guide the reader, we begin by examining simplified settings that illustrate how these conditions can be satisfied and explain why they are necessary.

Dimension of the parameterization The dimension P of the parameter space for kernels plays a key role. The lower P , the smaller both $\dim(\text{Im}(J(\bar{\theta})))$ and $\dim(\ker(J(\bar{\theta})))$, which in turn makes conditions (11) and (12) easier to fulfill. This is intuitive: with fewer parameters to identify, the system is more constrained, which generally increases identifiability.

Invertible convolutions and (10) Assume that $H_{\bar{\theta}}$ is invertible, that is, the Fourier transform of $h_{\bar{\theta}}$ does not vanish. In this case, (10) is automatically satisfied. We will discuss the non-invertible case later.

Linearly parameterized kernels and (11) Assume that h_1, \dots, h_P are elementary kernels and that $h_{\theta} = \sum_{p=1}^P \theta_p h_p$. For instance, if the kernels h_p are discrete Dirac delta functions located in a small neighborhood of the origin, this parameterization allows us to encode all compactly supported kernel. The Jacobian matrix $J(\theta)$ is independent of θ and writes $J(\theta) = [h_1 \star \bar{x}, \dots, h_P \star \bar{x}]$. Therefore, (11) only means that the elementary variations $h_p \star \bar{x}$ (e.g. shifted blurred images) are linearly independent.

Locally strongly convex prior and (12) If q is strongly convex around \bar{x} , then \bar{x} is a strict local minimizer of the potential. This hypothesis is not compatible with the intuition of an image manifold, where the prior would remain roughly constant along certain directions. Yet, this case is of interest since the conditions drastically simplify: (10) and (12) are automatically satisfied, since the Hessian of the potential is positive-definite. For instance, if a learned prior possesses local strict minimizers around each point in the training dataset, the images seen at training time would be the natural candidates to be recovered in inverse problems. Interestingly, in this case, the injectivity condition on $J(\bar{\theta})$ is sufficient to apply the theorem.

The general case The conditions in theorem 4 have a natural interpretation in terms of identifiability. Conditions (10) and (11) are local strong convexity condition for $\ell_{\bar{y}}(\bar{\theta}, \cdot)$ and $\ell_{\bar{y}}(\cdot, \bar{x})$ respectively. They ensure that given either \bar{x} or $\bar{\theta}$, the other can be recovered as a strict local minimizer of the corresponding loss. In particular (10) is classical: it ensures that when moving in any direction of the operator's $H_{\bar{\theta}}$ kernel, the potential increases. The condition (11) is an injectivity condition: it states that the blurred image should change when varying θ . A necessary condition is in particular that $\theta \mapsto h_{\theta}$ is injective. To the best of our knowledge, the condition (12) is novel. Intuitively, it can be understood as follows. Consider a small perturbation $(dx, d\theta)$ around the point $(\bar{x}, \bar{\theta})$. At first order, the synthesized image writes:

$$h_{\bar{\theta}+d\theta} \star (\bar{x} + dx) = \bar{y} + J(\bar{\theta})d\theta + h_{\bar{\theta}} \star dx + o(dx, d\theta).$$

If we can find a pair of directions $(d\theta, dx)$ such that, the synthesized image remains constant (that is $J(\bar{\theta})d\theta + h_{\bar{\theta}} \star dx = 0$) and the potential does not vary (that is $dx \in \ker \nabla^2 q(\bar{x})$), then the strict convexity of $\ell_{\bar{y}}$ is compromised. Condition (12) rules out this situation.

4 Numerical validation

Our aim in this section is to validate our theoretical findings in the previous section. First, we consider our univariate parameterized blur kernel families described in Section 2 and display, as a function of θ , the posterior value:

$$\ell_y^{\text{opt}}(\theta) \stackrel{\text{def}}{=} \inf_x \ell_y(x, \theta). \quad (13)$$

This allows us to explore the landscape of the joint posterior around natural images and around critical points. Second, we propose a MAP optimization strategy. It combines alternating updates on the image and on the kernel, combined

with a proper initialization strategy for the kernel and a re-initialization scheme for the image. We show that this strategy converges to satisfactory critical points of the posterior, corresponding to a local minimum, and avoids the no-blur solution.

4.1 Noise-free measurements

We first consider the noiseless case, that is $\bar{y} = H_{\bar{\theta}}\bar{x}$. We assume that H_{θ} is invertible for all θ in the range $[0, \theta_{\max}]$. This is achieved by considering slightly perturbed blur kernels $\tilde{h}_{\theta} = h_{\theta} + \lambda \text{Id}$, where λ is a small value and h_{θ} is the same as in fig. 5. The value of the hyperparameter λ for each blurring kernel family, is determined via grid search. These values are the smallest ones ensuring that the (pseudo-)inverse \tilde{H}_{θ}^{-1} satisfies:

$$\|x - \tilde{H}_{\theta}^{-1}y\| \leq 10^{-5} \quad \text{and} \quad q(x) \approx q(\tilde{H}_{\theta}^{-1}y), \quad (14)$$

where $y = \tilde{H}_{\theta}x$. We use the circular boundary condition of the convolution, so that the (pseudo-)inverse can be computed efficiently by leveraging the Fourier transform and the SVD decomposition, using the DeepInverse library [Tachella et al., 2025].

In this case, the infimum of $\ell_{\bar{y}}(\cdot, \theta)$ is given explicitly as $\hat{x}(\theta) = H_{\theta}^{-1}\bar{y}$. Hence, $\ell_{\bar{y}}^{\text{opt}}(\theta) = q(H_{\theta}^{-1}\bar{y})$, and the likelihood profile can be computed explicitly, see fig. 9.

We observe that the no-blur solution consistently minimizes the negative log-posterior, both when \bar{x} is sampled from the dataset and when it represents a critical point of the prior, supporting theorem 1. This experiment also supports theorem 4, confirming that the true image-kernel pair acts as a local minimizer of the negative log-posterior. Interestingly, we see that the motion and defocus kernels seem to be identifiable with much higher stability, since the profile is sharp around the true kernel's width. This is likely due to the fact that the Fourier transforms of these kernels vanish at a much slower rate than the ones associated to the Airy or Gaussian kernels. This makes the conditions of theorem 4 easier to fulfill. The curves for the Gaussian and Airy kernels around $\bar{\theta}$ shows that a local minimizer is present when starting from the critical points \bar{x}_i , but not when starting from the database images x_i . This is coherent with theorem 4.

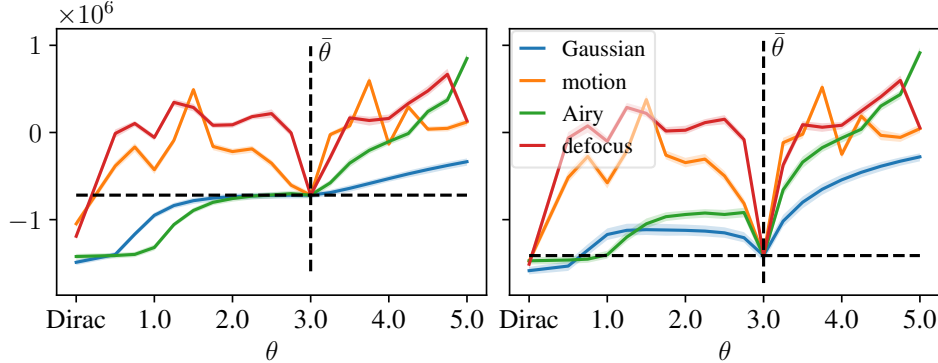


Figure 9: The function $\ell_{\bar{y}}^{\text{opt}}$ in (8) with noise-free measurements, using an FFHQ-256 model. Left: \bar{x} is from the dataset. Right: \bar{x} is a critical point of the prior. Observe that for critical points, the posterior has a local minimum around the true kernel $\bar{\theta}$, validating theorem 4.

4.2 Noisy measurement

In noisy scenarios ($\sigma_y > 0$), minimizing ℓ_y in (8) with respect to x becomes challenging. With neural network-parameterized priors, the posterior is highly non-convex. Nevertheless, $\ell_y^{\text{opt}}(\theta)$ can be approximated $\ell_y(\hat{x}(\theta), \theta)$, where $\hat{x}(\theta)$ is obtained by minimizing $x \mapsto \ell_y(x, \theta)$ with a first-order method. Our experiments employ gradient descent with momentum:

$$x_{k+1} = x_k - s \nabla_x \ell_y(x_k, \theta) + \beta(x_k - x_{k-1}), \quad \text{where } \beta \in [0, 1], s > 0. \quad (15)$$

We run this scheme from multiple initialization x_0 and retain the endpoint with the lowest potential.

Figure 10 illustrates ℓ_y^{opt} across different blur families and noise levels. At low noise levels, the posterior maintains a local minimizer near the true parameter $\bar{\theta}$, particularly when starting from a critical point of the prior. However, at higher noise levels, this minimizer vanishes, and the posterior decreases for smaller θ , biasing the model toward the no-blur solution. These findings strongly support theorem 5.

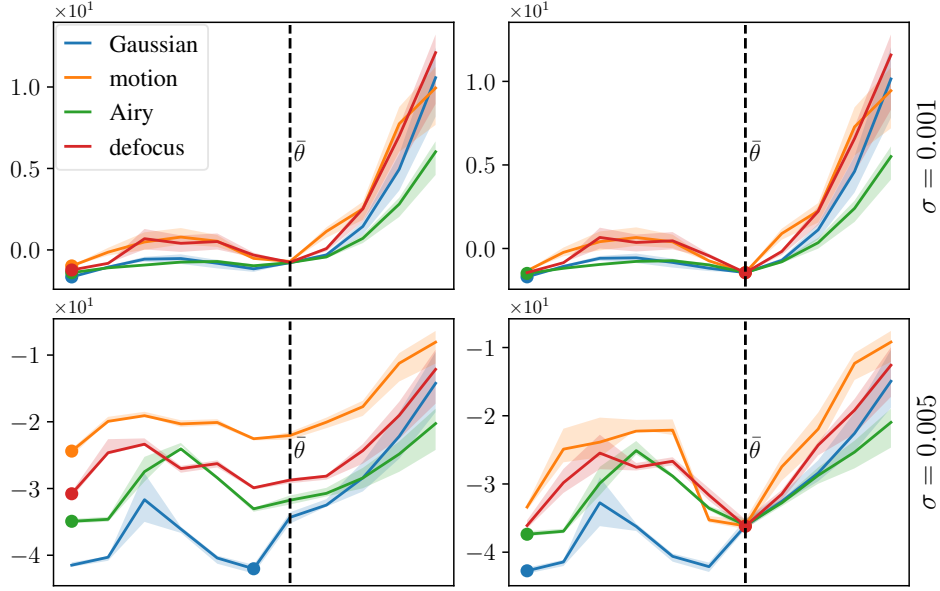


Figure 10: The function $\ell_y^{\text{opt}}(\theta)$ in (8) with noisy measurements for different noise levels. Left: \bar{x} is from the dataset. Right: \bar{x} is a critical point of the prior. Here, we used the FFHQ-256 model. This experiment supports theorem 5.

Algorithm 1 Blind deconvolution with alternating optimization

```

1: Input: blurry image  $y$ , number of alternating iterations  $K$ , number of iteration for image update  $K_x$ , step-size
 $\gamma_x, \gamma_\theta > 0$ .
2: Initialize  $\theta_0$  and  $x_0 = y$ 
3: for  $k = 0, 1, \dots, K - 1$  do
4:    $x_{k+1,0} = \begin{cases} y & \text{if } \text{mod}(k, 100) = 0 \\ x_{k,K_x} & \text{otherwise} \end{cases}$ 
   Minimization of the posterior with respect to the image
5:   for  $i = 0, 1, \dots, K_x - 1$  do
6:      $x_{k+1,i+1} = \text{prox}_{\gamma_x f(\cdot, \theta_k)}(x_{k+1,i} - \gamma_x \sigma_y^2 \nabla q(x_{k+1,i}))$ 
7:   end for
8:    $x_{k+1} = x_{k+1,K_x}$ 
   A gradient descent step for the kernel
9:    $\theta_{k+1} = \theta_k - \gamma_\theta \nabla_\theta f(x_{k+1}, \theta_k)$ 
10: end for
11: return  $x_K, \theta_K$ 

```

5 Initialization and optimization strategy for blind deconvolution

We now propose a simple heuristic, yet effective approach to initialize blind deblurring algorithms. This further validates theorem 5 and demonstrates empirically that the basin of attraction is sufficiently large along certain directions, making joint posterior minimization possible while avoiding the no-blur solution. The proposed method is based on the following 3 ideas:

1. *Initialization:* we initialize $x_0 = y$ and θ_0 such that $h(\theta_0)$ is the “largest” kernel in the family. This is motivated by the intuition that the basin of attraction is larger in the direction of larger kernels. Indeed, starting from a small kernel has good chances to converge to the global minimizer which is the no-blur solution.
2. *Optimization:* we do alternating optimization, but we perform several proximal gradient descent steps on the posterior with respect to x and only one gradient descent step with respect to θ (equivalently w.r.t to the kernel h) at each iteration.
3. *Re-initialization:* we reset $x_k = y$ regularly (e.g., when $k \equiv 0 \pmod{100}$) when the kernel $h(\theta_k)$ is updated. This can avoid the convergence to a bad local minimum.

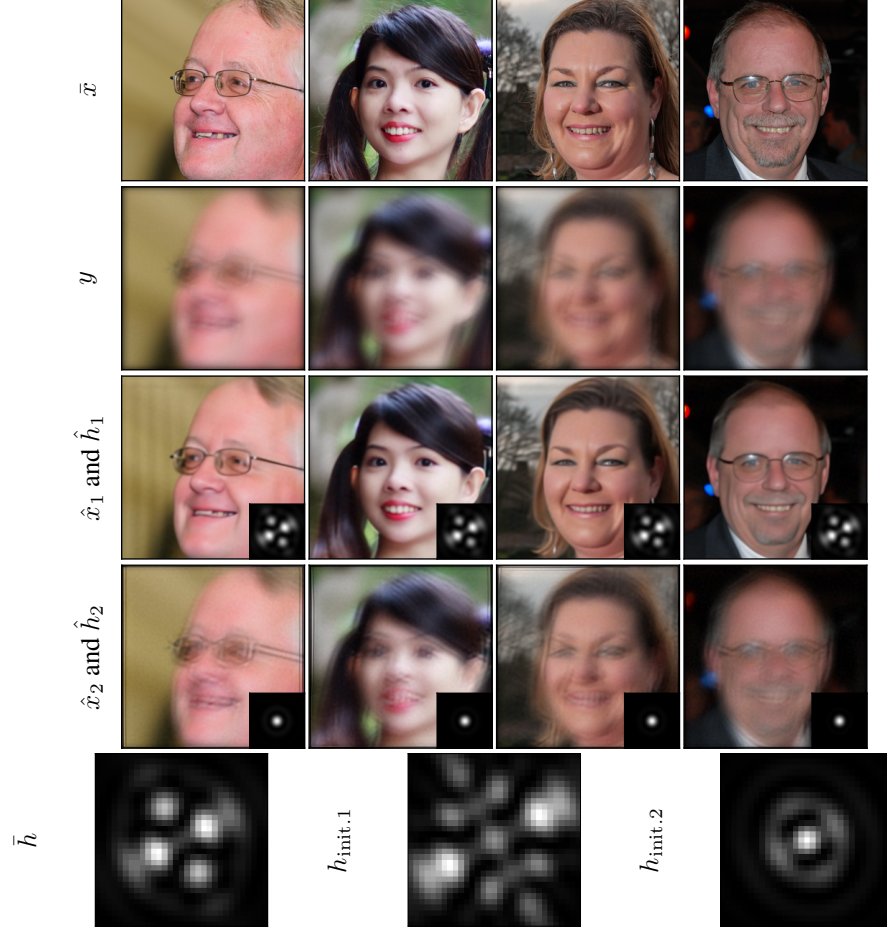


Figure 11: Example of joint posterior minimization for a diffraction-limited blur kernel. The algorithm 1 is initialized at y (observed with noise level $\sigma_y = 0.01$) and the kernels $h_{\text{init.1}}$ or $h_{\text{init.2}}$. The results for $h_{\text{init.1}}$ in the 3rd row is satisfactory, while the result for $h_{\text{init.2}}$ in the 4-th row is close to the no-blur solution. This illustrates the importance of initialization when minimizing the posterior jointly. Additional examples are given in Figure 14.

Let $f(x, \theta) = \frac{1}{2} \|h_\theta \star x - y\|^2$ denote the data fidelity term in the negative log posterior eq. (8). Our proposed strategy for minimizing eq. (8) is summarized in algorithm 1 and numerically validated in what follows. In this algorithm, the proximal operator $\text{prox}_{\gamma_x f(\cdot, \theta)}$ boils down to a linear system resolution, which can be efficiently computed using the conjugate gradient method. The gradient of the potential ∇q is computed using the score neural network and the gradient of the data fidelity term with respect to the kernel $\nabla_\theta f$ can be computed using automatic differentiation.

5.1 Parameterized blur kernels: diffraction-limited blurs

In this section, we are interested by diffraction-limited systems, which are essential in fields such as astronomy and microscopy. There, the PSF h_θ can be defined as the squared norm of the Fourier transform of the pupil function:

$$h_\theta = |\mathcal{F}(\exp(-i2\pi\phi_\theta))|^2, \quad (16)$$

where \mathcal{F} denotes the Fourier transform, and where the phase transition function $\phi_\theta : \mathbb{R}^2 \rightarrow \mathbb{R}$ is decomposed as a linear combination of Zernike polynomials z_p [Noll, 1976]: $\phi_\theta = \sum_{p=1}^P \theta_p z_p$, where $\theta \in \mathbb{R}^P$. Our experiments incorporate $P = 5$ typical optical aberrations: defocus, vertical/horizontal astigmatism, and primary spherical. We use the implementation from DeepInverse [Tachella et al., 2025]. In this parameterization, larger coefficients (in absolute value) in θ correspond to more complex PSFs. In other words, $h(\theta + \epsilon \cdot \text{sign}(\theta))$ is “simpler” (closer to an Airy pattern) than $h(\theta)$, when $\epsilon < 0$, and more “complex” than $h(\theta)$ when $\epsilon > 0$.

In fig. 11, we show that using a “large” (complex) initialization $h_{\text{init.1}} = h(\bar{\theta} + \epsilon \cdot \text{sign}(\bar{\theta}))$ with $\epsilon = 0.15$ consistently yields a near exact PSF recovery despite the noise. On the contrary, the smaller initialization $h_{\text{init.2}} = h(\bar{\theta} + \epsilon \cdot \text{sign}(\bar{\theta}))$

with $\epsilon = -0.1$ consistently converges to the Airy pattern (the smallest kernel in the family, corresponds to the no-blur solution). Other qualitative results are shown in fig. 14 in Appendix B where we observe the consistent convergence to the no-blur solution when using the smaller initialization, while the larger initialization leads to satisfactory results. All of these results are obtained with the algorithm 1 with $K_x = 100$, $K = 400$ iterations and $\gamma_x = 0.01$, $\gamma_\theta = 0.001$ and the FFHQ-256 model.

5.2 General blur kernels living in the simplex

We now consider a popular parameterization, where the kernel h_θ lives on the unit simplex. The mapping $\theta \in \mathbb{R}^P \mapsto h_\theta \in \mathbb{R}^P$ is the orthogonal projection of θ onto the simplex and P is the number of pixels of the kernel. We consider two simple initialization of the kernel:

- A “small” initialization: we consider a Gaussian kernel with standard-deviation of 1.5 pixels, as shown in fig. 12.
- A “large” initialization: we consider the largest possible kernel, which a uniform kernel in the spatial domain, as shown in fig. 12.

On synthetic data We first validate our initialization strategy on synthetic data. We consider 4 different blur kernels, including a diagonal motion blur, a motion blur from [Levin et al., 2011] and 2 diffraction-limited blur kernels.

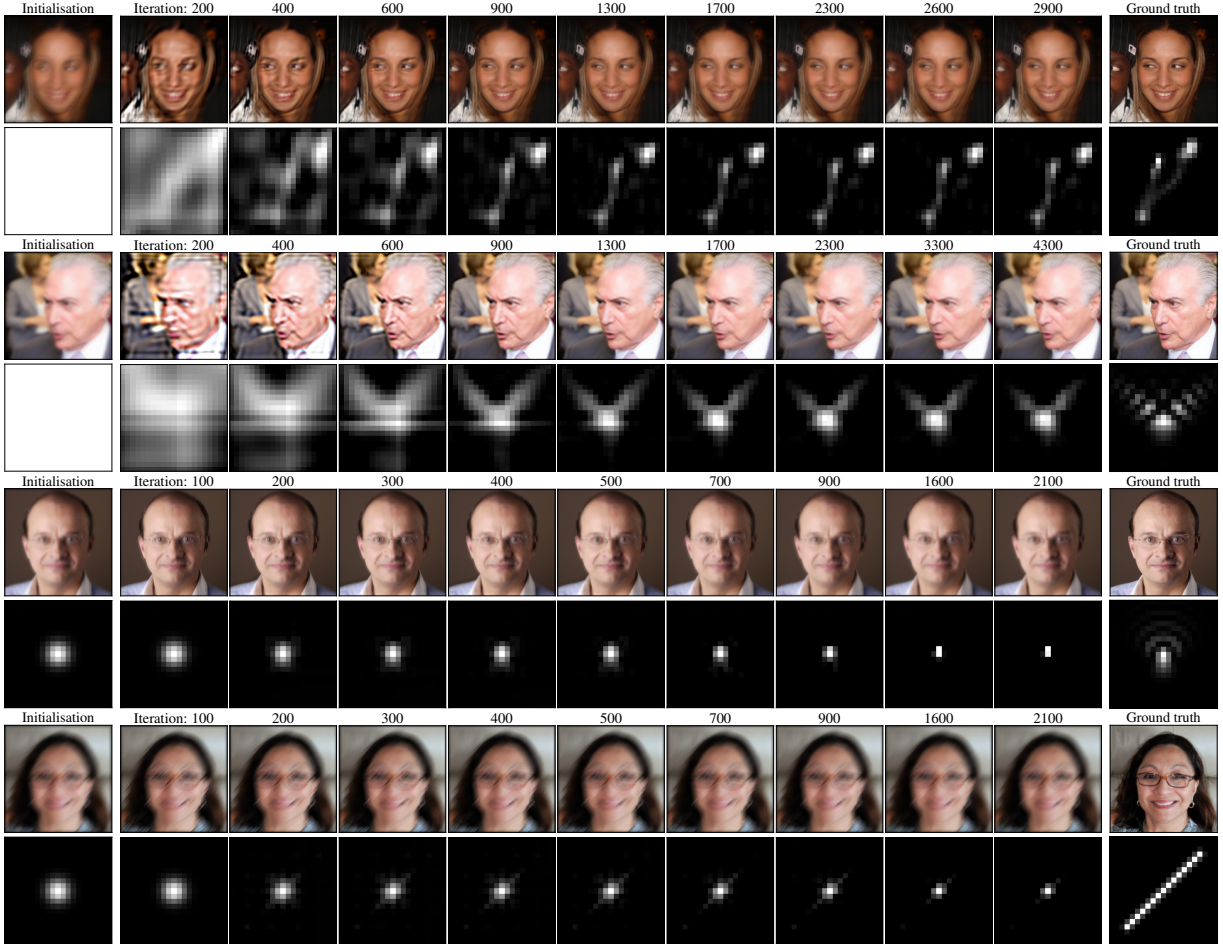


Figure 12: Illustration of the algorithm 1 and the influence of the kernel initialization $h(\hat{\theta}_0)$. A “large” initialization (uniform kernel, top two rows) of the kernel results in a satisfactory recovery of the image and the kernel. A “small” initialization (a Gaussian kernel with standard-deviation of 1.5, bottom two rows) of the kernel results in a convergence to the no-blur solution. We use the FFHQ-256 model from [Song et al., 2020].

The numerical results with the FFHQ-256 model are shown in fig. 12 and fig. 15 in Appendix B and illustrate the influence of the kernel initialization on the convergence of the algorithm. We observe that the “small” initialization leads to a convergence to the no-blur solution, while the “large” initialization leads to a satisfactory recovery of the image and the kernel. This is also coherent with the intuition that the basin of attraction is larger in the direction of larger kernels.

On real data To further validate our initialization strategy, we consider real data from the Köhler dataset [Köhler et al., 2012]. In this dataset, the motion-blurred images were generated by capturing a sequence of sharp images of static scenes while physically moving a real camera along controlled trajectories. The camera was mounted on a programmable platform that executed pre-defined two-dimensional motion paths. Each sharp frame in the sequence corresponds to an instantaneous camera position, and the motion-blurred image was computed as the temporal average of the sharp frames over the full exposure time, effectively simulating the integration of scene radiance along the camera trajectory. The pre-defined motion paths also allow us to compute the ground truth blur kernel, which allows comparing with the kernel recovered from our experiments.

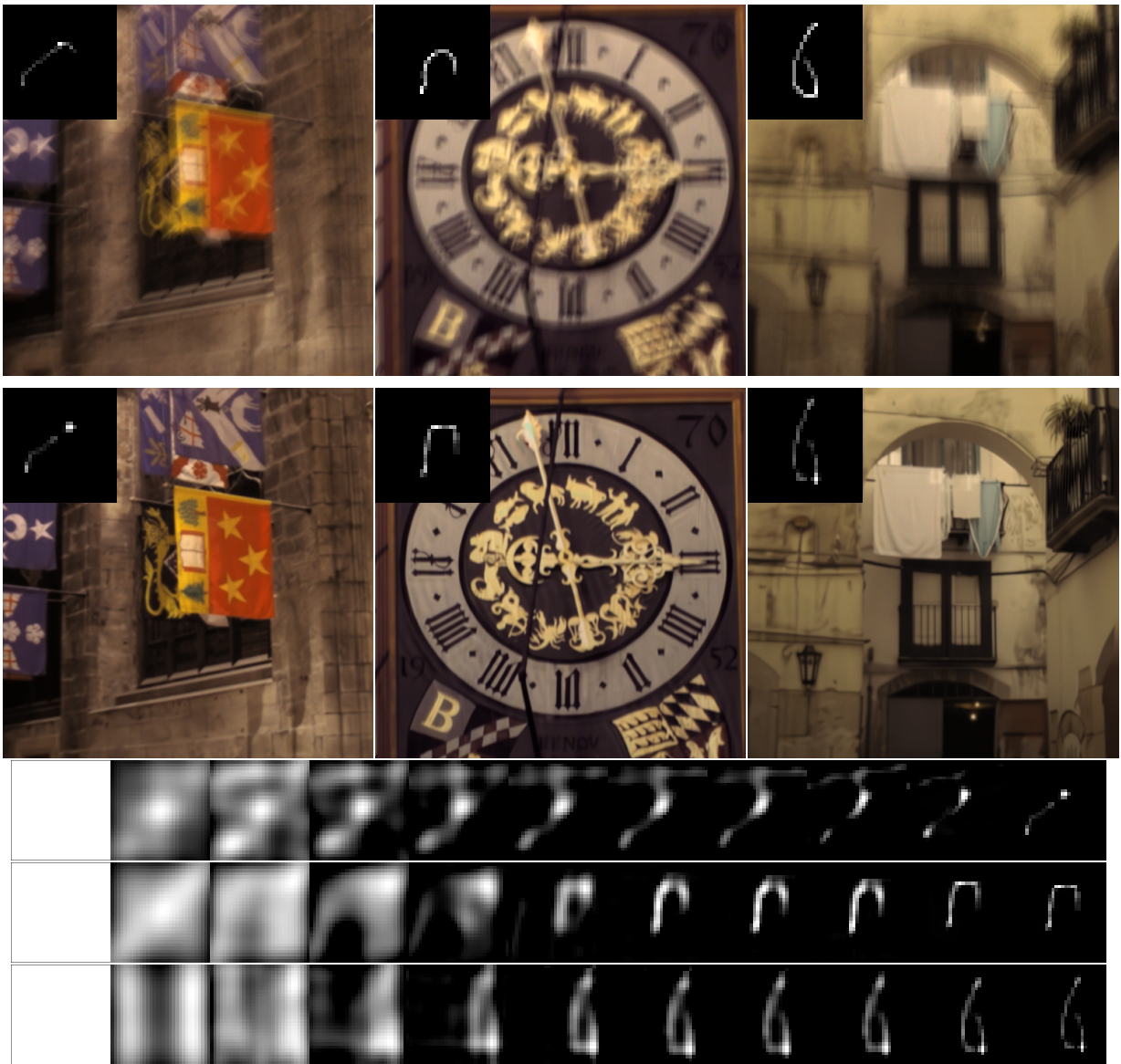


Figure 13: Results on the Köhler dataset [Köhler et al., 2012]. Top: real blurry images and true kernels. Middle: deblurred images and estimated kernels. Bottom: estimated kernel along iterations.

We show in fig. 13 the results on three different blurry images from the Köhler dataset [Köhler et al., 2012], with image crops of size 512×512 . Since there is no diffusion model trained on this dataset, we use the pretrained DRUNet denoiser [Zhang et al., 2021] as a prior for the image. We can interpret this denoiser either as a Maximum A Posteriori (MAP) estimator or as a Minimum Mean Squared Error (MMSE) estimator [Nguyen and Weiss, 2024]. Under the MAP interpretation, it corresponds to the proximal operator of a prior, while it also approximates the MMSE denoiser associated with a related—but distinct—prior [Gribonval, 2011]. In our experiments, we treat the DRUNet denoiser as the proximal operator of a prior and apply the Douglas-Rachford splitting method to minimize the joint posterior distribution over the image. Accordingly, line 6 in algorithm 1 is replaced with a Douglas-Rachford update step, as described in algorithm 2 of appendix B.

We initialize the kernel with a 51×51 uniform kernel and apply the algorithm 1. The results show that the algorithm is able to recover a satisfactory deblurred image and a good estimation of the kernel, illustrate the effectiveness of the proposed initialization and optimization strategy.

6 Conclusion

The Bayesian framework, with its principled approach of maximizing the joint posterior distribution, appears to be a natural choice for addressing blind deconvolution problems. However, our analysis reveals a surprising and fundamental limitation: the failure of MAP estimation, previously observed with handcrafted sparsity-based priors over the past two decades, persists even with state-of-the-art learned diffusion priors. This finding suggests that the limitations of MAP estimation in blind deconvolution are not only a consequence of inadequate priors, but rather an intrinsic characteristic of this bilinear inverse problem.

Nevertheless, we established precise conditions under which the joint posterior possesses local minima in the vicinity of the true solution, demonstrating that second-order critical points of the potential emerge as natural recovery points for MAP approaches in both blind and non-blind inverse problems. Our findings have important practical implications, particularly highlighting the crucial role of initialization in blind inverse problems. While global MAP estimation may be inherently problematic, our analysis suggests that Bayesian methods could still be effective for blind deconvolution. This message echoes existing results for handcrafted priors, and provides a clear guideline for the design of MAP based blind deconvolution: avoiding the no-blur solution requires careful initialization and possibly additional mechanisms to avoid undesired critical points.

Acknowledgments

The authors acknowledge a support from the ANR Micro-Blind ANR-21-CE48-0008 and from the ANR CLEAR-Microscopy. This work was performed using HPC resources from GENCI-IDRIS (Grant AD011012210).

References

- Tony F Chan and Chiu-Kwong Wong. Total variation blind deconvolution. *IEEE transactions on Image Processing*, 7(3):370–375, 1998.
- Jinshan Pan, Zhe Hu, Zhixun Su, and Ming-Hsuan Yang. Deblurring text images via l_0 -regularized intensity and gradient prior. In *Proceedings of the IEEE Conference on Computer Vision and Pattern Recognition*, pages 2901–2908, 2014.
- Joao P Oliveira, Mario AT Figueiredo, and Jose M Bioucas-Dias. Parametric blur estimation for blind restoration of natural images: Linear motion and out-of-focus. *IEEE Transactions on Image Processing*, 23(1):466–477, 2013.
- Adrian Shajkofci and Michael Liebling. Spatially-Variant CNN-Based Point Spread Function Estimation for Blind Deconvolution and Depth Estimation in Optical Microscopy. *IEEE Transactions on Image Processing*, 29:5848–5861, 2020.
- Valentin Debarnot and Pierre Weiss. Deep-blur: Blind identification and deblurring with convolutional neural networks. *Biological Imaging*, 2024.
- Jinshan Pan, Deqing Sun, Hanspeter Pfister, and Ming-Hsuan Yang. Blind image deblurring using dark channel prior. In *Proceedings of the IEEE conference on computer vision and pattern recognition*, pages 1628–1636, 2016.
- Di Ge, Jérôme Idier, and Eric Le Carpentier. Enhanced sampling schemes for mcmc based blind bernoulli–gaussian deconvolution. *Signal Processing*, 91(4):759–772, 2011.
- André Jalobeanu, Laure Blanc-Féraud, and Josiane Zerubia. Hyperparameter estimation for satellite image restoration using a mcmc maximum-likelihood method. *Pattern Recognition*, 35(2):341–352, 2002.

Nelly Pustelnik, Amel Benazza-Benhayia, Yuling Zheng, and Jean-Christophe Pesquet. Wavelet-based image deconvolution and reconstruction. *Wiley encyclopedia of electrical and electronics engineering*, 2016.

Jérémie Anger, Gabriele Facciolo, and Mauricio Delbracio. Blind Image Deblurring using the l_0 Gradient Prior. *Image Processing On Line*, 9:124–142, 2019. <https://doi.org/10.5201/ipol.2019.243>.

Anat Levin, Yair Weiss, Fredo Durand, and William T. Freeman. Understanding and evaluating blind deconvolution algorithms. In *2009 IEEE Conference on Computer Vision and Pattern Recognition*, pages 1964–1971, 2009. doi:10.1109/CVPR.2009.5206815.

Renu M Rameshan, Subhasis Chaudhuri, and Rajbabu Velmurugan. Joint map estimation for blind deconvolution: When does it work? In *Proceedings of the Eighth Indian Conference on Computer Vision, Graphics and Image Processing*, pages 1–7, 2012.

Daniele Perrone and Paolo Favaro. Total variation blind deconvolution: The devil is in the details. In *Proceedings of the IEEE Conference on Computer Vision and Pattern Recognition*, pages 2909–2916, 2014.

Alexis Benichoux, Emmanuel Vincent, and Rémi Gribonval. A fundamental pitfall in blind deconvolution with sparse and shift-invariant priors. In *2013 IEEE International Conference on Acoustics, Speech and Signal Processing*, pages 6108–6112. IEEE, 2013.

Robin Rombach, Andreas Blattmann, Dominik Lorenz, Patrick Esser, and Björn Ommer. High-resolution image synthesis with latent diffusion models. In *Proceedings of the IEEE/CVF conference on computer vision and pattern recognition*, pages 10684–10695, 2022.

Aditya Ramesh, Mikhail Pavlov, Gabriel Goh, Scott Gray, Chelsea Voss, Alec Radford, Mark Chen, and Ilya Sutskever. Zero-shot text-to-image generation. In *International Conference on Machine Learning*, pages 8821–8831. PMLR, 2021.

Tero Karras, Samuli Laine, and Timo Aila. A style-based generator architecture for generative adversarial networks. In *Proceedings of the IEEE/CVF conference on computer vision and pattern recognition*, pages 4401–4410, 2019.

Diederik P. Kingma and Max Welling. Auto-encoding variational bayes. In Yoshua Bengio and Yann LeCun, editors, *2nd International Conference on Learning Representations, ICLR 2014, Banff, AB, Canada, April 14-16, 2014, Conference Track Proceedings*, 2014. URL <http://arxiv.org/abs/1312.6114>.

Danilo Rezende and Shakir Mohamed. Variational inference with normalizing flows. In *International conference on machine learning*, pages 1530–1538. PMLR, 2015.

Yang Song, Jascha Sohl-Dickstein, Diederik P Kingma, Abhishek Kumar, Stefano Ermon, and Ben Poole. Score-based generative modeling through stochastic differential equations. In *International Conference on Learning Representations*, 2020.

Phil Pope, Chen Zhu, Ahmed Abdelkader, Micah Goldblum, and Tom Goldstein. The intrinsic dimension of images and its impact on learning. In *International Conference on Learning Representations*.

Tero Karras, Miika Aittala, Timo Aila, and Samuli Laine. Elucidating the design space of diffusion-based generative models. In *Proc. NeurIPS*, 2022.

Brian D.O. Anderson. Reverse-time diffusion equation models. *Stochastic Processes and their Applications*, 12(3):313–326, 1982. ISSN 0304-4149. doi:[https://doi.org/10.1016/0304-4149\(82\)90051-5](https://doi.org/10.1016/0304-4149(82)90051-5). URL <https://www.sciencedirect.com/science/article/pii/0304414982900515>.

Pascal Vincent. A connection between score matching and denoising autoencoders. *Neural computation*, 23(7):1661–1674, 2011.

Ricky TQ Chen, Yulia Rubanova, Jesse Bettencourt, and David K Duvenaud. Neural ordinary differential equations. *Advances in neural information processing systems*, 31, 2018.

John Skilling. *The Eigenvalues of Mega-dimensional Matrices*, pages 455–466. Springer Netherlands, Dordrecht, 1989. ISBN 978-94-015-7860-8. doi:10.1007/978-94-015-7860-8_48. URL https://doi.org/10.1007/978-94-015-7860-8_48.

Jason D Lee, Max Simchowitz, Michael I Jordan, and Benjamin Recht. Gradient descent only converges to minimizers. In *Conference on learning theory*, pages 1246–1257. PMLR, 2016a.

Adam Paszke, Sam Gross, Francisco Massa, Adam Lerer, James Bradbury, Gregory Chanan, Trevor Killeen, Zeming Lin, Natalia Gimelshein, Luca Antiga, Alban Desmaison, Andreas Köpf, Edward Yang, Zach DeVito, Martin Raison, Alykhan Tejani, Sasank Chilamkurthy, Benoit Steiner, Lu Fang, Junjie Bai, and Soumith Chintala. *PyTorch: an imperative style, high-performance deep learning library*. Curran Associates Inc., Red Hook, NY, USA, 2019.

Jakiw Pidstrigach. Score-based generative models detect manifolds. *Advances in Neural Information Processing Systems*, 35:35852–35865, 2022.

Jan Paweł Stanczuk, Georgios Batzolis, Teo Deveney, and Carola-Bibiane Schönlieb. Diffusion models encode the intrinsic dimension of data manifolds. In *Forty-first International Conference on Machine Learning*, 2024.

Rafal Karczewski, Markus Heinonen, and Vikas Garg. Diffusion models as cartoonists: The curious case of high density regions. In *The Thirteenth International Conference on Learning Representations*, 2025. URL <https://openreview.net/forum?id=RiS2cxpENN>.

Ali Ahmed, Benjamin Recht, and Justin Romberg. Blind deconvolution using convex programming. *IEEE Transactions on Information Theory*, 60(3):1711–1732, 2013.

Kiryung Lee, Yanjun Li, Marius Junge, and Yoram Bresler. Blind recovery of sparse signals from subsampled convolution. *IEEE Transactions on Information Theory*, 63(2):802–821, 2016b.

Michael Kech and Felix Krahmer. Optimal injectivity conditions for bilinear inverse problems with applications to identifiability of deconvolution problems. *SIAM Journal on Applied Algebra and Geometry*, 1(1):20–37, 2017.

Ashish Bora, Ajil Jalal, Eric Price, and Alexandros G Dimakis. Compressed sensing using generative models. In *International conference on machine learning*, pages 537–546. PMLR, 2017.

Hyungjin Chung, Jeongsol Kim, Sehui Kim, and Jong Chul Ye. Parallel diffusion models of operator and image for blind inverse problems. In *Proceedings of the IEEE/CVF Conference on Computer Vision and Pattern Recognition*, pages 6059–6069, 2023.

Hamadi Chihaoui, Abdelhak Lemhenter, and Paolo Favaro. Blind image restoration via fast diffusion inversion. *arXiv preprint arXiv:2405.19572*, 2024.

Feng Li, Yixuan Wu, Zichao Liang, Runmin Cong, Huihui Bai, Yao Zhao, and Meng Wang. Blinddiff: Empowering degradation modelling in diffusion models for blind image super-resolution. *arXiv preprint arXiv:2403.10211*, 2024.

Yash Sanghvi, Yiheng Chi, and Stanley H Chan. Kernel diffusion: An alternate approach to blind deconvolution. In *ECCV*, 2025.

Charles Laroche, Andrés Almansa, and Eva Coupete. Fast diffusion EM: a diffusion model for blind inverse problems with application to deconvolution. In *Proceedings of the IEEE/CVF Winter Conference on Applications of Computer Vision*, pages 5271–5281, 2024.

Julián Tachella, Matthieu Terris, Samuel Hurault, Andrew Wang, Dongdong Chen, Minh-Hai Nguyen, Maxime Song, Thomas Davies, Leo Davy, Jonathan Dong, Paul Escande, Johannes Hertrich, Zhiyuan Hu, Tobías I. Liaudat, Nils Laurent, Brett Levac, Mathurin Massias, Thomas Moreau, Thibaut Modrzyk, Brayan Monroy, Sebastian Neumayer, Jérémie Scanvic, Florian Sarron, Victor Sechaud, Georg Schramm, Romain Vo, and Pierre Weiss. Deepinverse: A python package for solving imaging inverse problems with deep learning, 2025. URL <https://arxiv.org/abs/2505.20160>.

Robert J Noll. Zernike polynomials and atmospheric turbulence. *JOSA*, 66(3):207–211, 1976.

Anat Levin, Yair Weiss, Fredo Durand, and William T. Freeman. Efficient marginal likelihood optimization in blind deconvolution. In *CVPR 2011*, pages 2657–2664, 2011. doi:10.1109/CVPR.2011.5995308.

Rolf Köhler, Michael Hirsch, Betty Mohler, Bernhard Schölkopf, and Stefan Harmeling. Recording and playback of camera shake: Benchmarking blind deconvolution with a real-world database. In *Computer Vision–ECCV 2012: 12th European Conference on Computer Vision, Florence, Italy, October 7–13, 2012, Proceedings, Part VII 12*, pages 27–40. Springer, 2012.

Kai Zhang, Yawei Li, Wangmeng Zuo, Lei Zhang, Luc Van Gool, and Radu Timofte. Plug-and-play image restoration with deep denoiser prior. *IEEE Transactions on Pattern Analysis and Machine Intelligence*, 44(10):6360–6376, 2021.

Minh Hai Nguyen and Pierre Weiss. Comparing Plug-and-Play and Unrolled networks. working paper or preprint, September 2024. URL <https://hal.science/hal-04703008>.

Rémi Gribonval. Should penalized least squares regression be interpreted as maximum a posteriori estimation? *IEEE Transactions on Signal Processing*, 59(5):2405–2410, 2011.

A Proof

A.1 Proof of theorem 1

Theorem 6. Let $\mathcal{H} = \{h_\theta, \theta \in \mathbb{R}^P\}$ denote the set of blur kernels. If the Dirac delta function $\delta \in \mathcal{H}$ and for any image x and kernel $h \in \mathcal{H}$,

$$q(h \star x) \leq q(x), \quad (17)$$

Consider the negative log-posterior minimization problem:

$$\min_{x, \theta} \frac{1}{2} \|H_\theta x - y\|^2 + \sigma^2 q(x). \quad (18)$$

Then the set of global minimizers of (18), if non-empty, contains the Dirac kernel and the MAP denoised image.

Proof. Let (\hat{x}, \hat{h}) be a solution to (18). If $\hat{h} \neq \delta$, we can replace (\hat{x}, \hat{h}) with $(\hat{h} \star \hat{x}, \delta)$ and get a lower cost function. Indeed, the point $(\hat{h} \star \hat{x}, \delta)$ does not modify the value of the data fidelity term in (18) and since we assumed that $q(\hat{x}) \geq q(\hat{h} \star \hat{x})$, $(\hat{h} \star \hat{x}, \delta)$ is also a solution. This shows that the Dirac kernel is a solution to the joint MAP problem. If the inequality were strict in (17), the solution would be unique and satisfy $\hat{h}_{\text{MAP}} = \delta$. Note that when \hat{h}_{MAP} is the Dirac mass, the estimated image coincides with a MAP-denoised image:

$$\hat{x}_{\text{MAP}}(y) = \arg \min_x \frac{1}{2} \|x - y\|_2^2 + \sigma^2 q(x). \quad (19)$$

□

A.2 Generalization of the main theoretical results for linear blind inverse problems

This section provides stability guarantees for general blind linear inverse problems. The main mechanism to solve invariance under-termination is to leverage prior information on the image x , through a prior density function, and A through its parameterization. We start by the following lemma which characterizes the positiveness of a block matrix.

Lemma 7. Let the matrix

$$N = \begin{pmatrix} A & J \\ D & 0 \end{pmatrix}$$

have a zero kernel, and D be positive semi-definite, then the following is positive-definite.

$$M = \begin{pmatrix} A^T A + D & A^T J \\ J^T A & J^T J \end{pmatrix}$$

This happens if and only if $\ker J = \{0\}$, $A \ker D \cap \text{Im } J = \{0\}$ and $\ker D \cap \ker A = \{0\}$.

Proof. Since D is semi-definite, it has a symmetric semi-definite square root \sqrt{D} such that $D = \sqrt{D} \sqrt{D}$. Set

$$L = \begin{pmatrix} A & J \\ \sqrt{D} & 0 \end{pmatrix}$$

we have $M = L^T L$, so that it is positive semi-definite. Furthermore, D and \sqrt{D} have the same kernel, so that $\ker M = \ker L = \ker N = \{0\}$ and M is positive-definite.

For the last part, if $\ker J \neq \{0\}$ or $A \ker D \cap \text{Im } J \neq \{0\}$ or $\ker D \cap \ker A \neq \{0\}$ then $\ker N \neq \{0\}$. Now assuming they are all null, for any $(u, v) \in \ker N$, $u \in \ker D$ and $Au + Jv = 0$ so that $Jv \in A \ker D \cap \text{Im } J$, $Jv = 0$ and $v = 0$. □

The main theoretical result presented in theorem 4 and theorem 5 is in fact a particular case of a more general linear blind inverse problem in the following theorem.

Theorem 8. Consider $A: \mathbb{R}^P \rightarrow \mathbb{R}^{M \times N}$ a \mathcal{C}^2 parameterized family of operators, and $g: \mathbb{R}^N \rightarrow \mathbb{R}$ a \mathcal{C}^2 prior function. Fix $\bar{x} \in \mathbb{R}^N$, $\bar{y} \in \mathbb{R}^M$ and $\bar{\theta} \in \mathbb{R}^P$ such that

$$\nabla g(\bar{x}) = 0 \quad \nabla^2 g(\bar{x}) \succeq 0 \quad A(\bar{\theta})\bar{x} = \bar{y}.$$

Set for all $\theta \in \mathbb{R}^P$, $J(\theta) = \frac{\partial}{\partial \theta}(A(\theta)\bar{x}) \in \mathbb{R}^{M \times P}$ and assume the following

$$\begin{aligned} \ker \nabla^2 g(\bar{x}) \cap \ker A(\bar{\theta}) &= \{0\}, \quad \ker J(\bar{\theta}) = \{0\}, \\ \text{and} \quad (A(\bar{\theta}) \ker \nabla^2 g(\bar{x})) \cap \text{Im } J(\bar{\theta}) &= \{0\}. \end{aligned}$$

Then there exists $r, \epsilon > 0$ and two Lipschitz functions $\Delta_x: \mathcal{B}(0, \epsilon) \rightarrow \mathbb{R}^N$ and $\Delta_\theta: \mathcal{B}(0, \epsilon) \rightarrow \mathbb{R}^P$ such that $\Delta_x(0) = 0$, $\Delta_\theta(0) = 0$, and for any $b \in \mathcal{B}(0, \epsilon) \subset \mathbb{R}^M$, $(\bar{x} + \Delta_x(b), \bar{\theta} + \Delta_\theta(b))$ is a strict local minimizer of the objective function

$$\begin{aligned} \ell_b: \mathbb{R}^P \times \mathbb{R}^N &\rightarrow \mathbb{R} \\ (x, \theta) &\mapsto \frac{1}{2} \|A(\theta)x - (\bar{y} + b)\|^2 + g(x). \end{aligned}$$

This minimizer is the unique critical point in $\mathcal{B}((\bar{x}, \bar{\theta}), r)$.

Proof. We let J_A denote the Jacobian of A , such that $A(\theta + \dot{\theta}) \approx A(\theta) + J_A(\theta) \cdot \dot{\theta}$, where $J_A(\theta) \in \mathcal{L}(\mathbb{R}^P, \mathbb{R}^{M \times N})$. We use the notation $J_A(\theta) \stackrel{\text{def}}{=} [\partial_1 A(\theta), \dots, \partial_P A(\theta)]$ where we write $\partial_p = \frac{\partial}{\partial \theta_p}$ for brevity of the directional derivative with respect to θ_p . Furthermore, we use the following convention, for any $\dot{\theta} \in \mathbb{R}^P$ and $C \in \mathbb{R}^{M \times N}$, we define:

$$J_A(\theta) \cdot \dot{\theta} \stackrel{\text{def}}{=} \sum_{p=1}^P \dot{\theta}_p \partial_p A(\theta) \in \mathbb{R}^{M \times N}$$

and

$$J_A^T(\theta) \cdot C \stackrel{\text{def}}{=} \begin{pmatrix} \langle \partial_1 A(\theta), C \rangle_{M \times N} \\ \vdots \\ \langle \partial_P A(\theta), C \rangle_{M \times N} \end{pmatrix} \in \mathbb{R}^P,$$

as the operator of the Jacobian and its adjoint, respectively. For any vector $x \in \mathbb{R}^N$, consider the mapping

$$\theta \in \mathbb{R}^P \mapsto Q_x(\theta) = A(\theta)x \in \mathbb{R}^M$$

The Jacobian of Q_x is given by:

$$J_{Q_x}(\theta) = (\partial_1 A(\theta) \cdot x, \dots, \partial_P A(\theta) \cdot x) \in \mathbb{R}^{M \times P}.$$

We have $J = J_{Q_{\bar{x}}}$ for J as given in the statement. For any b , we let $y = \bar{y} + b$. We use the notation $z = (x, \theta) \in \mathbb{R}^{N+P}$ and rewrite the cost function $\ell_b(z) = f(z) + g(z)$ where:

$$f(z) = \frac{1}{2} \|A(\theta)x - y\|_2^2 \quad \text{and} \quad g(z) = g(x). \quad (20)$$

First order derivatives We have

$$\begin{aligned} \nabla_x f(z) &= A^T(\theta) [A(\theta)x - y] \\ \nabla_\theta f(z) &= \begin{pmatrix} \langle \partial_1 A(\theta) \cdot x, A(\theta)x - y \rangle_{\mathbb{R}^M} \\ \vdots \\ \langle \partial_P A(\theta) \cdot x, A(\theta)x - y \rangle_{\mathbb{R}^M} \end{pmatrix} = J^T(\theta) (A(\theta)x - y) \end{aligned}$$

Second order derivatives We have

$$\begin{aligned} \partial_{x,x} f(z) &= A^T(\theta) A(\theta) \\ (\partial_{\theta,\theta}^2 f(z))_{p,q} &= \langle \partial_{p,q} A(\theta) \cdot x, A(\theta)x - y \rangle + \langle \partial_p A(\theta) \cdot x, \partial_q A(\theta) \cdot x \rangle \\ \partial_{x,\theta} f(z) &= \begin{pmatrix} (\partial_1 A(\theta))^T (A(\theta)x - y) \\ \vdots \\ (\partial_P A(\theta))^T (A(\theta)x - y) \end{pmatrix}^T + A^T(\theta) J(\theta) \end{aligned}$$

where $\partial_{p,q} = \frac{\partial^2}{\partial \theta_p \partial \theta_q} \in \mathbb{R}^{M \times N}$ is the (p, q) -th directional derivative of A .

The noiseless case Let $\bar{z} = (\bar{x}, \bar{\theta})$ with $A(\bar{\theta})\bar{x} = \bar{y}$ as in the statement. In that situation, we may choose $b = 0$, $y = \bar{y}$, we obtain the following expression for the Hessian of f at \bar{z} ,

$$\nabla_z^2 f(\bar{z}) = \begin{pmatrix} \partial_{x,x} f(\bar{z}) & \partial_{x,\theta} f(\bar{z}) \\ \partial_{\theta,x} f(\bar{z}) & \partial_{\theta,\theta} f(\bar{z}) \end{pmatrix} = \begin{pmatrix} A^T(\bar{\theta})A(\bar{\theta}) & A^T(\bar{\theta})J(\bar{\theta}) \\ J^T(\bar{\theta})A(\bar{\theta}) & J^T(\bar{\theta})J(\bar{\theta}) \end{pmatrix}$$

Then the Hessian of ℓ reads:

$$\nabla^2 \ell_0(\bar{z}) = \begin{pmatrix} A^T(\bar{\theta})A(\bar{\theta}) + \nabla^2 g(\bar{x}) & A^T(\bar{\theta})J(\bar{\theta}) \\ J^T(\bar{\theta})A(\bar{\theta}) & J^T(\bar{\theta})J(\bar{\theta}) \end{pmatrix} \quad (21)$$

By Lemma 7, this matrix is positive-definite. By continuity of the eigenvalues and twice continuous differentiability of ℓ , there exists $\mu > 0$ and $r > 0$ such that $\nabla^2 h(z) \succeq \mu I$ for all $z \in \mathcal{B}(\bar{z}, r)$.

The general case For an arbitrary b , we have

$$\ell_b(z) = \ell_0(z) - \langle A(\theta)x - \bar{y}, b \rangle + \frac{1}{2}\|b\|^2$$

The second derivative $\nabla^2 \ell_b - \nabla^2 \ell_0$ depends linearly on b and continuously on z . Since $\nabla^2 \ell_0(z) \geq \mu I$ on $\mathcal{B}(\bar{z}, r)$, for ϵ small enough, reducing μ if necessary, we have that for any b such that $\|b\| \leq \epsilon$, the function ℓ_b is μ strongly convex on $\mathcal{B}(\bar{z}, r)$.

The gradient of ℓ_b reads

$$\nabla \ell_b(z) = \nabla \ell_0(z) - \begin{pmatrix} A^T(\theta)b \\ J_{Q_x}^T(\theta)b \end{pmatrix}$$

Set

$$M = \max_{z \in \mathcal{B}(\bar{z}, r), \|b\| \leq 1} \sqrt{\|A^T(\theta)b\|^2 + \|J_{Q_x}^T(\theta)b\|^2}$$

Let $z \in \partial \mathcal{B}(\bar{z}, r)$, and $\|b\| \leq \frac{\mu r}{M}$, we have:

$$\begin{aligned} & \langle \nabla \ell_b(z), z - \bar{z} \rangle \\ &= \langle \nabla \ell_0(z), z - \bar{z} \rangle - \left\langle \begin{pmatrix} A^*(\theta)b \\ J_{Q_x}^T(\theta)b \end{pmatrix}, z - \bar{z} \right\rangle \\ &\geq \mu \|z - \bar{z}\|^2 - \sqrt{\|A^T(\theta)b\|^2 + \|J_{Q_x}^T(\theta)b\|^2} \cdot \|z - \bar{z}\| \\ &= \mu r^2 - r \sqrt{\|A^T(\theta)b\|^2 + \|J_{Q_x}^T(\theta)b\|^2} \\ &= r(\mu r - M\|b\|) \\ &\geq 0. \end{aligned}$$

By the Brouwer's fixed point theorem, there exists $z_b^* \in \mathcal{B}(\bar{z}, r)$ such that $\nabla \ell_b(z_b^*) = 0$. Indeed, let us argue by contradiction and assume that this is not the case. Up to a translation and scaling, we may assume that $r = 1$ and $\bar{z} = 0$. The mapping $z \mapsto \frac{-\nabla \ell_b(z)}{\|\nabla \ell_b(z)\|}$ is continuous from the unit ball into itself. It has therefore a fixed point satisfying $z = \frac{-\nabla \ell_b(z)}{\|\nabla \ell_b(z)\|} \in \partial \mathcal{B}(0, 1)$ and $\langle z, \nabla \ell_b(z) \rangle = -\|\nabla \ell_b(z)\| < 0$ which is contradictory with the preceding inequality.

By strong convexity of ℓ_b on $\mathcal{B}(\bar{z}, r)$, z_b^* is the unique minimizer of ℓ_b on the ball. We have by μ -strong convexity of ℓ_b for any b, b' with norm at most ϵ ,

$$\begin{aligned} \mu \|z_b^* - z_{b'}^*\|^2 &\leq \langle \nabla \ell_b(z_{b'}^*) - \nabla \ell_b(z_b^*), z_{b'}^* - z_b^* \rangle \\ &= \langle \nabla \ell_b(z_{b'}^*), z_{b'}^* - z_b^* \rangle \\ &\leq \|\nabla \ell_b(z_{b'}^*)\| \|z_{b'}^* - z_b^*\| \\ &\leq M \|b\| \|z_{b'}^* - z_b^*\| \end{aligned}$$

So that in $\|z_b^* - z_{b'}^*\| \leq \frac{M}{\mu} \|b\|$. We can define Δ_x and Δ_θ such that for all b , $\|b\| \leq \epsilon$, $(\Delta_x(b), \Delta_\theta(b)) = z_b^* - \bar{z}$. \square

B Additional experiments

Algorithm 2 Blind deconvolution with alternating optimization — Douglas-Rachford splitting method

```

1: Input: blurry image  $y$ , a denoiser  $D$ , number of alternating iterations  $K$ , number of iteration for image update  $K_x$ , step-size  $\gamma_x, \gamma_\theta > 0$ .
2: Initialize  $\theta_0$  and  $x_0 = y$ 
3: for  $k = 0, 1, \dots K - 1$  do
4:    $x_{k+1,0} = \begin{cases} y & \text{if } \text{mod}(k, 100) = 0 \\ x_{k,K_x} & \text{otherwise} \end{cases}$ 
   Minimization of the posterior with respect to the image
5:   for  $i = 0, 1, \dots K_x - 1$  do
6:      $z = D(x_{k+1,i})$ 
7:      $x_{k+1,i+1} = x_{k+1,i} + \text{prox}_{\gamma_x f(\cdot, \theta_k)}(2z - x_{k+1,i}) - z$ 
8:   end for
9:    $x_{k+1} = x_{k+1,K_x}$ 
   A gradient descent step for the kernel
10:   $\theta_{k+1} = \theta_k - \gamma_\theta \nabla_\theta f(x_{k+1}, \theta_k)$ 
11: end for
12: return  $x_K, \theta_K$ 

```

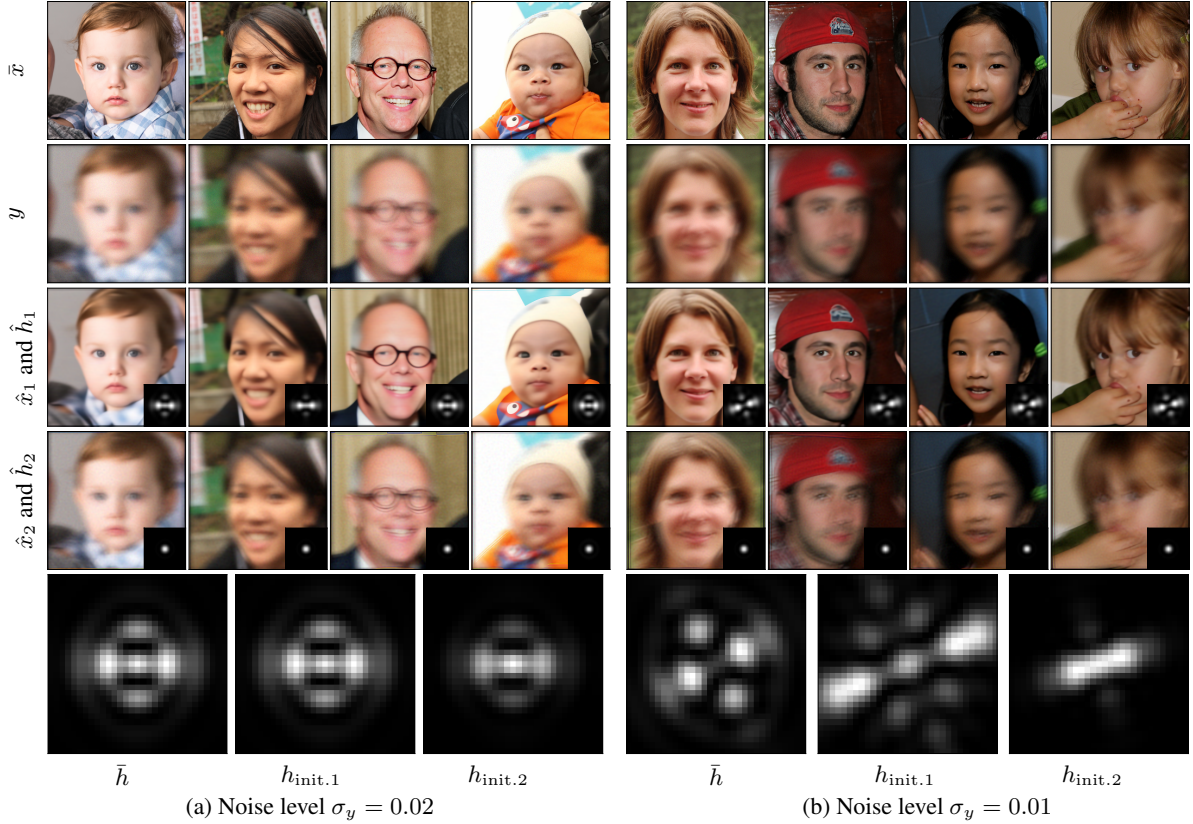


Figure 14: More examples on the influence of initialization for blind deconvolution, with diffraction-limited blur kernels as in Figure 11. The initialization are $h_{\text{init.}1} = h(\theta + 0.15 \cdot \text{sign}(\bar{\theta}))$ and $h_{\text{init.}2} = h(\theta - 0.075 \cdot \text{sign}(\bar{\theta}))$ and $x_0 = y$. Again, using large kernels for initialization leads to a decent kernel reconstruction, while small kernels lead to the no-blur solution.

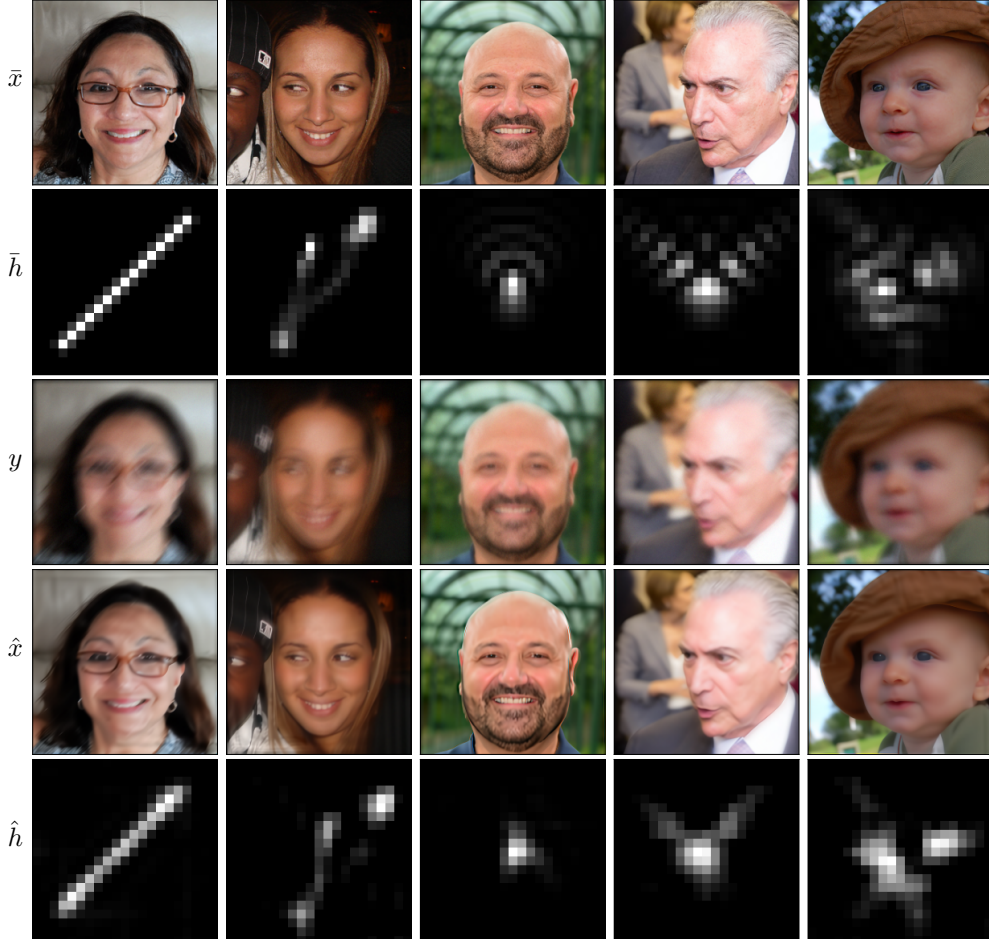


Figure 15: More numerical results with a simplex constraint using different pairs (\bar{x}, \bar{h}) , similarly as fig. 12. The algorithm algorithm 1 is initialized by a uniform kernel. The noise level is $\sigma = 0.01$. The kernel's shape is recovered approximately and the estimated images look sharper.